

RESEARCH ARTICLE

REM1.3's phospho-status defines its plasma membrane nanodomain organization and activity in restricting PVX cell-to-cell movement

Artemis Perraki¹[✉][¶], Julien Gronnier¹[¶][‡], Paul Gouguet¹, Marie Boudsocq²[¶], Anne-Flore Deroubaix¹, Vincent Simon³, Sylvie German-Retana³, Anthony Legrand^{1,4}[¶], Birgit Habenstein⁴[¶], Cyril Zipfel^{5,6}[¶], Emmanuelle Bayer¹[¶], Sébastien Mongrand^{1*}[¶], Véronique Germain¹

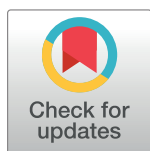
1 Laboratoire de Biogenèse Membranaire (LBM), UMR 5200, CNRS/Université de Bordeaux, Bordeaux, France, **2** Institute of Plant Sciences Paris Saclay (IPS2), CNRS, INRA, Université Paris-Sud, Université d'Evry, Université Paris-Saclay, Université Paris-Diderot, Sorbonne Paris-Cité, Plateau du Moulon, France, **3** Equipe de Virologie UMR BFP 1332 INRA, Villenave d'Ornon, France, **4** Institute of Chemistry & Biology of Membranes & Nanoobjects (UMR5248 CBMN), IECB, CNRS, Université de Bordeaux, Institut Polytechnique de Bordeaux, All. Geoffroy Saint-Hilaire, Pessac, France, **5** The Sainsbury Laboratory, Norwich Research Park, Norwich, United Kingdom, **6** Institute of Plant and Microbial Biology and Zürich-Basel Plant Science Center, University of Zürich, Zürich, Switzerland

 These authors contributed equally to this work.

[✉] Current address: Department of Plant Sciences, University of Cambridge, Cambridge, United Kingdom

[‡] Current address: Institute of Plant and Microbial Biology and Zürich-Basel Plant Science Center, University of Zürich, Zürich, Switzerland.

* sebastien.mongrand@u-bordeaux.fr



OPEN ACCESS

Citation: Perraki A, Gronnier J, Gouguet P, Boudsocq M, Deroubaix A-F, Simon V, et al. (2018) REM1.3's phospho-status defines its plasma membrane nanodomain organization and activity in restricting PVX cell-to-cell movement. PLoS Pathog 14(11): e1007378. <https://doi.org/10.1371/journal.ppat.1007378>

Editor: Aiming Wang, Agriculture and Agri-Food Canada, CANADA

Received: July 5, 2018

Accepted: October 3, 2018

Published: November 12, 2018

Copyright: © 2018 Perraki et al. This is an open access article distributed under the terms of the [Creative Commons Attribution License](https://creativecommons.org/licenses/by/4.0/), which permits unrestricted use, distribution, and reproduction in any medium, provided the original author and source are credited.

Data Availability Statement: All relevant data are within the paper and its Supporting Information files are available from Arabidopsis Genome Initiative (<https://www.arabidopsis.org/index.jsp>), and GenBank/EMBL (<https://www.ncbi.nlm.nih.gov/genbank/>) databases under the accession numbers: StREM1.3 (NP_001274989), AtREM1.2 (At3g61260), AtREM1.3 (At2g45820), AtCPK3 (At4g23650).

Abstract

Plants respond to pathogens through dynamic regulation of plasma membrane-bound signaling pathways. To date, how the plant plasma membrane is involved in responses to viruses is mostly unknown. Here, we show that plant cells sense the Potato virus X (PVX) COAT PROTEIN and TRIPLE GENE BLOCK 1 proteins and subsequently trigger the activation of a membrane-bound calcium-dependent kinase. We show that the *Arabidopsis thaliana* CALCIUM-DEPENDENT PROTEIN KINASE 3-interacts with group 1 REMORINS *in vivo*, phosphorylates the intrinsically disordered N-terminal domain of the Group 1 REMORIN REM1.3, and restricts PVX cell-to-cell movement. REM1.3's phospho-status defines its plasma membrane nanodomain organization and is crucial for REM1.3-dependent restriction of PVX cell-to-cell movement by regulation of callose deposition at plasmodesmata. This study unveils plasma membrane nanodomain-associated molecular events underlying the plant immune response to viruses.

Author summary

Viruses propagate in plants through membranous channels, called plasmodesmata, linking each cell to its neighboring cell. In this work, we challenge the role of the plasma

Funding: AP was supported by the Greek fellowship program IKY, <https://www.iky.gr/en/>. JG, PG and AFD were supported by the Ministère de l'Enseignement Supérieur et de la Recherche, France (doctoral grants), <http://www.enseignementsup-recherche.gouv.fr/cid76053/le-financement-doctoral.html>. MB was supported by LabEx Saclay Plant Sciences-SPS (ANR-10-LABX-0040-SPS), <https://www6.inra.fr/saclay-plant-sciences>. VG, SM, EB, VS VG were supported by the French ANR project "Potymove" (ANR-16-CE20-008-01), <http://www.agence-nationale-recherche.fr/en/>. EB, VG and SM were supported by ANR project (CE19_2014_CONNECT) <http://www.agence-nationale-recherche.fr/en/>. CZ was supported by Gatsby Charitable Foundation, <http://www.gatsby.org.uk> and the European Research Council (grant "PHOSPHinnATE"), <https://erc.europa.eu>. The funders had no role in study design, data collection and analysis, decision to publish, or preparation of the manuscript.

Competing interests: The authors have declared that no competing interests exist.

membrane in the regulation of virus propagation. By studying the dynamics and the activation of a plant-specific protein called REMORIN, we found that the way this protein is organized inside the membrane is crucial to fulfill its function in the immunity of plants against viruses.

Introduction

The cell plasma membrane (PM) constitutes a regulatory hub for information processing [1]. Current knowledge suggests that PM proteins and lipids dynamically associate with each other to create specialized sub-compartments or nanodomains [2], that regulate the cellular responses in space and time [3–5]. For instance, modeling of the localization behavior of a PM-bound receptor and its downstream interactor before and after ligand perception in animal cells suggests that PM-partitioning into nanodomains improves the reliability of cell signaling [6]. In plants a recent example of PM partitioning shows that despite sharing several signaling components, the immune and growth receptors FLS2 and BRI1 are divided into context-specific nanodomains to confer signaling specificity [7]. The REMORIN (REM) family is one of the best-characterized PM nanodomain-associated proteins in plants [7–12]. The association of REMs to the PM is mediated by a short sequence at the extremity of the C-terminus of the protein, called REM-CA (REMORIN C-terminal Anchor) [13, 14]. The REM C-terminal domain contains a coiled-coil (residues 117–152, [15]) which is thought to regulate REM oligomerization [11, 14, 16] and may be involved in regulating REM spatial organization at the PM [15]. Members of the REM family have been associated with plant responses to biotic [9, 17, 18], abiotic stress [19, 20] and developmental cues [12] and current view suggests they could regulate signaling events through nanodomain association [21]. However, the molecular mechanisms leading to REM-associated downstream events remain elusive.

Several REM proteins have been identified as components of the plasmodesmata-plasma membrane subcompartment (PD-PM) [8, 22, 23]. PD are membranous nanopores, crossing the plant cell wall and enabling cytoplasmic, endoplasmic reticulum and PM continuity between adjacent cells. They regulate the intercellular transport of proteins and small molecules during development and defense [24, 25]. The PD-PM is a particular subcompartment of the PM, which displays a unique molecular composition, notably enriched in sterols [26]. The movement of macromolecules through PD can be tightly controlled through modulation of the PD size-exclusion limit (SEL) *via* hypo- or hyper-accumulation of callose at the PD neck region [27–29]. Overexpression of GRAIN SETTING DEFECT 1 (GSD1) encoding a phylogenetic-group 6 REM protein from rice, restricts PD aperture and transport of photo-assimilates [23].

PDs are also the only route available for plant viruses to spread from cell-to-cell. *Potato virus X* (PVX) promotes its cell-to-cell movement *via* modification of PD permeability [30] through the action of TRIPLE GENE BLOCK PROTEIN 1 (TGBp1) [31]. Overexpression of *StREM1.3* (*Solanum tuberosum* REM from group 1b, homolog 3 [32], further referred as REM1.3) hampers TGBp1's ability to increase PD permeability [33]. How REM1.3 obstructs TGBp1 action is still unknown. Here, we used REM1.3 and PVX pathosystem in the solanaceae *Nicotiana benthamiana*, because PVX cannot infect *Arabidopsis* [34] and *N. benthamiana* is a widely used model for research on plant-virus interaction [35]. We previously showed that REM1.3 lateral organization into nanodomains at the PM is directly linked with its ability to restrict PVX movement and regulate PD conductance [36].

REM1.3 was the first REM family member discovered and initially described as a protein phosphorylated upon treatment with oligogalacturonides, which are plant cell wall components and elicitors of plant defense [37, 38]. The biological relevance of REM phosphorylation is not known of different REM phospho-statuses suggest that the activity of these proteins could be regulated by phosphorylation during plant-microbe interactions [16, 17, 39, 40].

In the present paper, we show that phosphorylation of REM dictates its membrane dynamics and antiviral defense by the reduction of PD permeability. Our data point towards a model in which viral proteins such as the Coat Protein (CP), TGBp1 from PVX and 30K proteins from *Tobacco mosaic virus* (TMV) elicit the activation of protein kinase(s), which in turn phosphorylate(s) REM1.3 at its N-terminal domain. In turn, REM1.3's phospho-status regulates its spatial-temporal organization at the PM and association with PD. The latter is associated with PD closure by induction of callose deposition at PD pit fields and restriction of viral cell-to-cell movement. Last, we further provide evidence that the membrane bound *Arabidopsis* CALCIUM-DEPENDENT PROTEIN KINASE 3 (CPK3) interacts with the taxonomic group 1b REMs *in vivo*, phosphorylates REM1.3 *in vitro* and restricts PVX propagation in a REM-dependent manner. Collectively, this study brings valuable information about the involvement of PM nanodomains dynamics during the establishment of membrane-bound signaling processes.

Results

PVX triggers changes in REM1.3's membrane dynamic behavior and REM1.3 association with plasmodesmata

Group 1 and group 6 REM have been described as proteins regulating PD size-exclusion limit [8, 23, 33]. REM1.3 plays a role in restricting PVX passage through PD channels [8], [33] counteracting PVX movement proteins which promote PD opening [41]. To study the potential function of REM1.3 at PD in response to PVX infection, we surveyed simultaneously PD callose content and REM1.3 PD localization in healthy or PVX-infected *N. benthamiana* transiently expressing YFP-REM1.3 [42] (S1 Fig). Our analysis showed a significant increase in callose deposition in PVX-infected cells compared to mock conditions (Fig 1A and 1B). This finding suggests the recognition of PVX-encoded elicitors and the mobilization of a plant defense response leading to an increase of callose accumulation at PD pit fields.

Since protein activation is often linked to changes in subcellular localization [3, 44], we next examined whether PVX infection triggers changes in REM1.3 association with PD. Calculation of the PD index (ratio between fluorescence intensity of YFP-REM1.3 at the aniline-labeled PD pit fields and fluorescence at the PM around the pit fields [28], S1 Fig). Fig 1A and 1B showed that despite its role on PD regulation, YFP-REM1.3 is not enriched in the PD region of healthy *N. benthamiana* epidermal cells. We however reproducibly observed a slight increase of YFP-REM1.3 PD index upon PVX infection suggesting that PVX perception modulates REM1.3 localization and association with the PD pitfields (Fig 1A and 1B).

To gain further insights into REM1.3 dynamic localization at the PM upon PVX infection, we applied single-particle tracking Photoactivated Localization Microscopy in Variable Angle Epifluorescence Microscopy mode (spt-PALM VAEM) in living *N. benthamiana* epidermal cells [45] in absence or presence of PVX. We used the photoconvertible fluorescent protein EOS [46, 47] fused to REM1.3 to visualize, track, and characterize mobility behavior of single REM1.3 molecules. In addition, nanoscale localizations of single molecules observed overtime were computed to obtain super-resolution images and analyze REM1.3 organization at a molecular level. By this approach, we recently studied the protein organization and mobility parameters of single EOS-REM1.3 molecules in non-infected conditions and found that

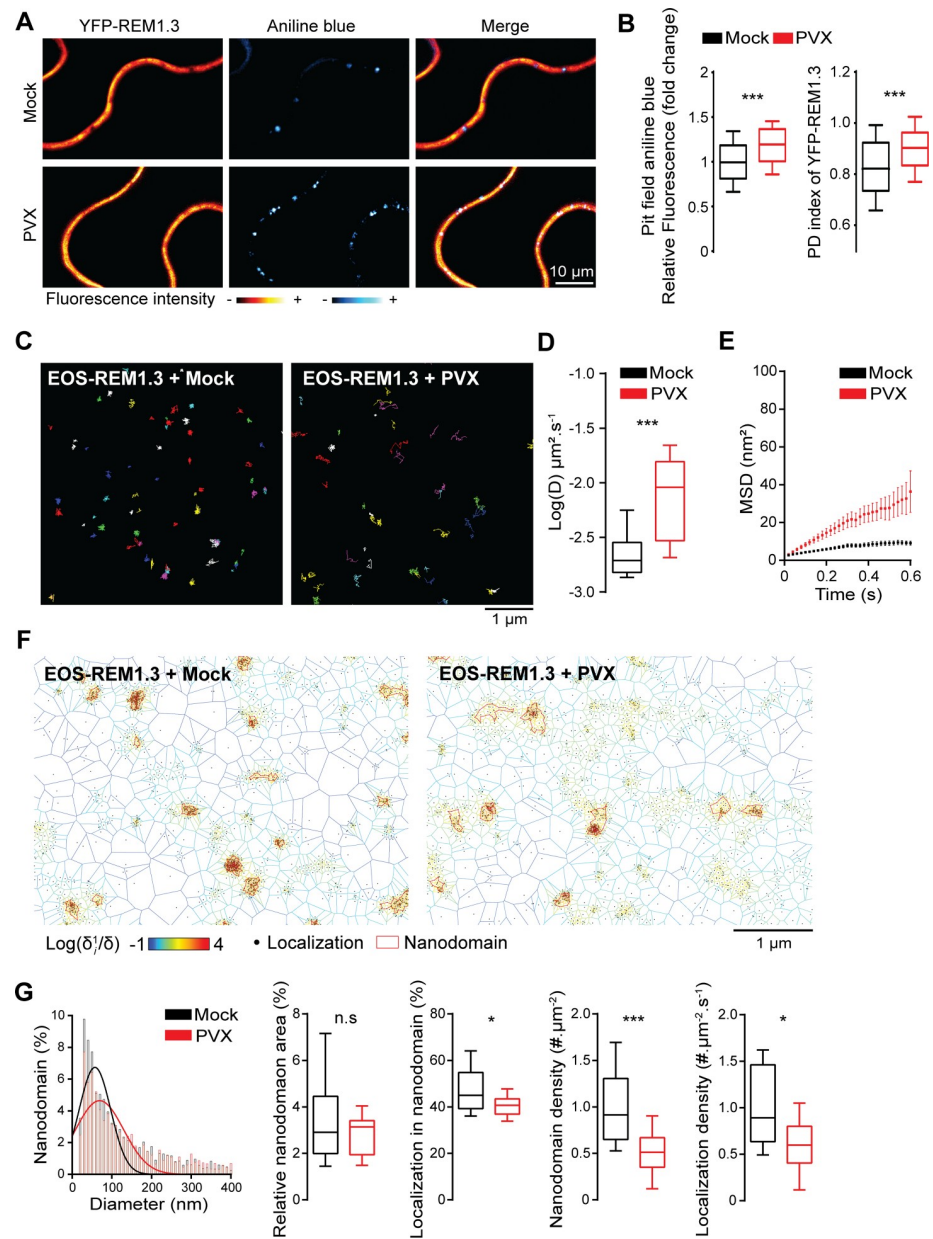


Fig 1. REM1.3 modulates plasmodesmata callose accumulation and displays altered PM organization and dynamic following PVX infection. (A) Representative confocal images of aniline blue stained *N. benthamiana* leaf epidermal cells transiently expressing YFP-REM1.3 in the absence (mock is infiltration with empty *A. tumefaciens*) or the presence of PVX at 2 days after infiltration (DAI). Color-coding indicates fluorescence intensity. (B) *Left*, Pit field aniline blue fluorescence intensity was quantified by ImageJ as described in S1 Fig and expressed as the percentage of the mock control. *Right*, Quantification of the PD residency of YFP-REM1.3 in the absence (mock) and in the presence of PVX using the PD index [28] as described in S1 Fig. Graphs represent quantifications from 3 independent biological experiments. At least 15 cells per condition were analysed per experiment. Significant differences were determined by Mann-Whitney comparisons test *** $p < 0.001$. (C) Super-resolved trajectories of EOS-REM1.3 molecules (illustrated by different colours) in the PM plane in the absence (Mock) and presence of PVX obtained by high-resolution microscopy spt-PALM. EOS-REM1.3 was transiently expressed in *N. benthamiana* (D) Diffusion coefficients (D) of EOS-REM1.3 expressed as log(D) in the absence (Mock) and presence of PVX. Statistical significances were assessed by Mann-Whitney test *** $p < 0.001$ using data collected over two independent experiments. (E) Mean Square Displacement (MSD) over time for the global trajectories of EOS-REM1.3 followed during at least 600 ms reflecting two independent experiments. (F) Live PALM analysis of EOS-REM1.3 localization in the absence (mock) and presence of PVX by tessellation-based automatic segmentation of super-resolution images. (G) Computation of EOS-REM1.3 single molecule organization features based on tessellation-based automatic segmentation images. For

REM1.3 nanodomain size distribution for the indicated conditions, the Gaussian fits in absence (mock) and presence of PVX are indicated by lines. Total nanodomain area is expressed as percentage of the total PM surface. Percentage of EOS-REM1.3 molecules localizing into nanodomains, relative to all molecules observed. Localization density refers to the number of molecules observed per μm^2 per second. Statistics were performed on at least 10 data sets per condition, from two independent experiments. Significant differences were determined by Mann-Whitney test * $p < 0.05$, *** $p < 0.001$.

<https://doi.org/10.1371/journal.ppat.1007378.g001>

EOS-REM1.3 displays an immobile and confined PM localization pattern, as commonly observed for plant membrane-associated proteins (Fig 1C–1E) [48], [36]. Reminiscent of these data, previous studies using different techniques described REM-associated PM domains to be predominantly laterally static [36, 48, 49]. Analysis of PVX-infected cells demonstrated an increase of EOS-REM1.3 diffusion coefficient (D) and mean square displacement (MSD), reflecting an increase of REM1.3 mobility (Fig 1C–1E). We next apply mathematical computation (Voronoi tessellation method [36, 50]) to compare the supra-molecular organization of EOS-REM1.3 of live PALM data in mock- and PVX-infected conditions (Fig 1F and 1G). Computation of EOS-REM1.3 single molecule organization features demonstrated a modulation of REM1.3 nanodomain-organization upon PVX infection (Fig 1G). Following PVX infection, the EOS-REM1.3-formed nanodomains are bigger in size, and there is a slight decrease of the proportion of molecules that localized into nanodomains as well as a decrease in the number of nanodomains formed. Overall, in both conditions, EOS-REM1.3 nanodomains represented similar proportions of the total PM surface. Additionally, a decrease in the localization density (number of molecules observed per μm^2 per s) showed that upon PVX infection, there was less REM1.3 protein at the PM level. Overall, the changes of REM1.3 distribution under PVX infection *i.e.* enrichment of YFP-REM1.3 in the PD pit field regions, the increase of REM1.3's mobility and the modulation of REM1.3 nanodomain organization, suggest that the plant cell modulates PD-PM and PM nanodomain dynamics to circumvent PVX infection.

Perception of PVX proteins by plant cells leads to the activation of kinase (s) phosphorylating REM1.3

REM1.3 overexpression restricts PVX local and systemic spreading in both *Solanum lycopersicum* [8] and *Nicotiana benthamiana* [33, 36] (S2A and S2B Fig). Because REM1.3 protein level is not affected by PVX infection (S2C and S2D Fig), we assumed that neither synthesis nor degradation of the protein is modified by PVX, but perhaps post-translational modifications. As REM1.3 was originally discovered as a PM-associated phosphorylated protein [38], we first asked whether REM1.3 could be phosphorylated by leaf protein extracts. Equal protein amounts of microsomal and soluble extracts from *N. benthamiana* leaves were used as a potential kinase source to phosphorylate affinity-purified full-length 6His-REM1.3 in an *in vitro* kinase assay in the presence of ATP [γ - ^{33}P]. Autoradiography revealed the presence of a clear band corresponding to a phosphorylated form of 6His-REM1.3 by kinase(s) present in the microsomal fraction (Fig 2A). The intensity of this band was completely abolished by competition with cold ATP, but not cold AMP, indicating a valid experimental set-up to study a genuine transphosphorylation event (S3A Fig). Phosphorylation of 6His-REM1.3 was almost undetectable in soluble fractions, representing cytosolic kinases (Fig 2A). *In silico* analysis predicted phosphorylation sites throughout REM1.3 sequence (Diphos, DEPP and NETPHOS prediction softwares). In agreement with the location of the sites presenting the highest phosphorylation potential, we experimentally found that REM1.3 was phosphorylated in its N-terminal domain (residues 1–116, hereafter 6His:REM1.3^N) whereas the C-terminal domain

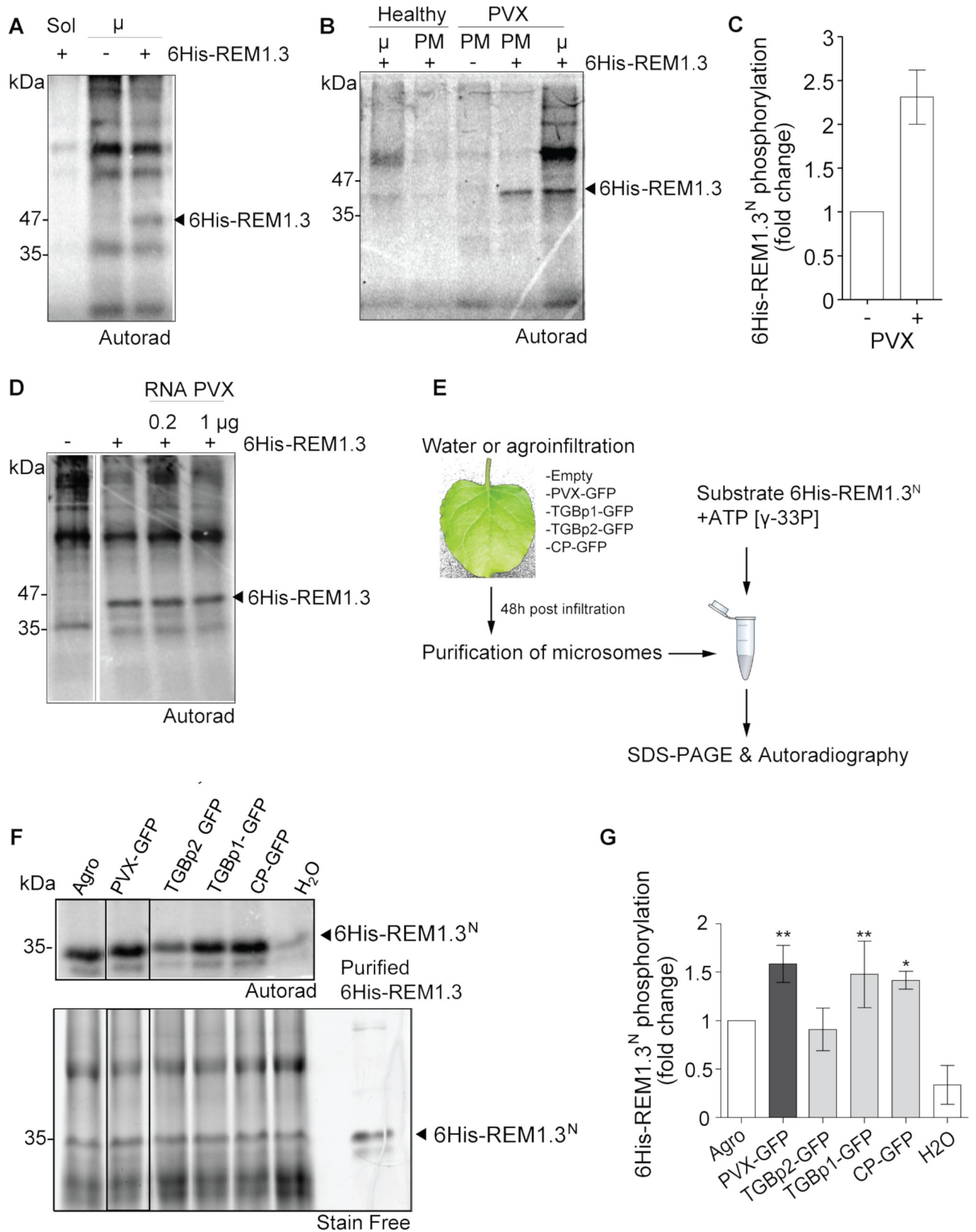


Fig 2. PVX and viral proteins induce REM1.3 phosphorylation in its N-terminal domain. (A, B) *In vitro* protein phosphorylation assays were performed by incubation of recombinant affinity-purified 6His-REM1.3 and *N. benthamiana* extracts with [γ - ^{33}P]-ATP. The samples were run on SDS-PAGE gels and developed by autoradiography. Soluble (Sol) or microsomal (μ) extracts of healthy leaves in (A), or microsomal and PM extracts from healthy and PVX-infected plants in (B) were used. (C) *In vitro* phosphorylation of 6His-REM1.3^N by leaf microsomal extracts of healthy or PVX-infected *N. benthamiana* leaves. Bars show the quantification of phosphorylated 6His-REM1.3N bands from 5 independent repeats. (D) *In vitro* phosphorylation of 6His-REM1.3 by leaf microsomal extracts in the presence of total RNA extracts from PVX-infected leaves. (E) Experimental flow-chart to study the role virus protein in membrane-bound kinase activation. (F) 6His-REM1.3N phosphorylation by microsomal extracts infected with PVX-GFP or expressing the indicated viral proteins at 4 DAI. Leaves expressing GFP alone, infiltrated with water or with *A. tumefaciens* strain GV3101 alone served as controls. Expression of the viral proteins is presented in S3 Fig. (G) Graph represents the quantification of 6His-REM1.3N bands from three independent repeats (n = 3), as a percentage of the activity induced by *A. tumefaciens* strain GV3101 alone. Error bars show SE, and significance is assessed by Dunnett's multiple comparison test to water control (*, P < 0.1; **, P < 0.05; ***, P < 0.001). Phosphorylated proteins were detected by autoradiography and total proteins by stain free procedure. In all experiments 10 μg of total protein extracts and 1 μg of affinity purified 6His-REM1.3 or 6His-REM1.3^N were loaded per lane.

<https://doi.org/10.1371/journal.ppat.1007378.g002>

(residues 117–198, hereafter 6His:REM1.3^C) did not present any detectable phosphorylation (S3B and S3C Fig).

We next tested whether PVX activates the kinase(s) that phosphorylate(s) REM1.3. Our results unveiled that microsomal and PM fractions extracted from symptomatic PVX-infected leaves promoted higher levels of 6His-REM1.3 phosphorylation compared to non-infected plants (Fig 2B and 2C). Studies have shown that functionally different viral components, such as virus-encoded proteins and double-stranded RNA, can trigger plant defense responses [51–56]. We therefore examined whether the PVX genome in its free form was an eliciting signal for kinase activation. We found that the addition of total RNAs extracted from PVX-infected plants in the kinase reaction mix did not alter the levels of 6His-REM1.3 phosphorylation (Fig 2D). We then examined whether the sole expression of individual viral movement proteins was sufficient to trigger REM1.3 phosphorylation (Fig 2E). Importantly, our results demonstrated that the expression of TGBp1 and Coat Protein (CP) fused to GFP triggered the strongest levels of 6His-REM1.3^N phosphorylation to the same extent as the full PVX-GFP construct (Fig 2F and 2G and S3E Fig for controls of viral fluorescent-tagged protein expression as described in [41]). In good agreement, expression of a TGBp1-deleted version of PVX (PVX Δ TGBp1) decreased 6His-REM1.3 phosphorylation levels compared to wild-type PVX extracts (S3D Fig). Expression of TGBp2 and infiltration of the empty *Agrobacterium* strain alone protein also induced 6His-REM1.3^N phosphorylation, albeit less effective than TGBp1 and CP proteins (Fig 2F and 2G). In accordance with previous reports suggesting REM phosphorylation during plant-microbe interactions [9], *Agrobacterium* infected *N. benthamiana* extracts induced much stronger REM1.3 phosphorylation than the water control condition (Fig 2F and 2G). Furthermore, we found that the 30K-RFP protein from Tobacco mosaic virus (TMV) also induces REM phosphorylation (S3D Fig). Similar to PVX-TGBp1, REM1.3 interferes with the ability of TMV-30K to increase PD permeability [33] and overexpression of REM1.3 restricts TMV-GFP cell-to-cell movement in *N. benthamiana* epidermal cells (S4A Fig).

Altogether our data suggest an additional role of REM-mediated plant response against TMV and possibly to bacteria. Our results also indicate that REM1.3 phosphorylation status is modulated by the perception of viral proteins by plant cells.

Phosphorylation of REM1.3 regulates its function in restricting PVX spreading via PD aperture modulation

Since phosphorylation of REM occurs upon PVX infection, we next aimed to functionally characterize the importance of REM1.3 phosphorylation for the regulation of PVX cell-to-cell movement. Despite our efforts, the identification of *in vivo* phosphorylation sites of REM1.3 appeared technically challenging and remained unsuccessful. *In silico* predictions and *in vitro*

kinase assays however showed that REM1.3^N displays regions of intrinsic disorder and presents the highest potential of phosphorylation (Fig 2C–2F and Fig 3A). For functional characterization, we selected the three putative phosphorylation Serine(S)/Threonine(T) sites present in REM1.3^N, namely S74, T86 and S91, that presented high scores of phosphorylation prediction in intrinsic disorder regions (Fig 3A). S74 and S91 are conserved across the phylogenetic group 1b of REM proteins, suggesting functional redundancy (S5A Fig) [32, 57]. S74 and S91 were the analogous residues identified as phosphorylated *in vivo* in the group 1b REM *AtREM1.3* (At2g45820) of *Arabidopsis thaliana* (hereafter *Arabidopsis*) in a stimuli-dependent manner [39, 40, 57]. Biochemical analysis showed that α -1,4-poly-D-galacturonic acid (PGA)-induced phosphorylation of *StREM1.3* occurs on T32, S74 and T86 [58]. T86 is not conserved in *Arabidopsis* but it is conserved in Solanaceae REM proteins, such as in *N. benthamiana* (S5A Fig). By an *in vitro* kinase assay, we show that phosphorylation occurs within three potential phosphor-residues, since mutation of S74, T86 and S91 to the non-phosphorylatable Aspartic acid (D), generating the 6His-REM1.3^{DDD} mutant abolished REM phosphorylation by the PVX-activated kinase(s) (Fig 3B and 3C).

To discriminate which residues are functionally relevant in the context of PVX-GFP propagation, we generated RFP-tagged REM1.3 phosphomutants, individually mutated at those sites to the non-phosphorylatable Alanine. Transient expression in *N. benthamiana* coupled with PVX-GFP infection assays demonstrated that individual phospho-null mutations at those sites induce a loss of function of REM1.3 in restricting PVX-GFP spreading (Fig 3D). This result suggests that phosphorylation of either S74, T86 and S91 is important for REM1.3 function.

To further characterize the relevance of different REM1.3 phospho-statuses in the context of PVX-GFP propagation and PD-aperture regulation, we analysed RFP-tagged REM1.3^{DDD} to mimic constitutive phosphorylation hereafter termed phosphomimetic mutant, or to Alanine (REM1.3^{AAA}) hereafter termed phosphodead mutant. Infection assays in *N. benthamiana* confirmed that the phosphodead mutant completely lost REM1.3 ability to restrict PVX-GFP cell-to-cell movement, while the phosphomimetic mutant maintained this ability (Fig 3D). TMV-GFP propagation was similarly affected by the phospho-status of REM1.3 (S4A Fig). We then analyzed the capacity of REM1.3 phosphomutants to regulate PD aperture in the absence of viral infection. As previously described [33, 36], RFP-REM1.3 reduces the PD size-exclusion limit as measured by free-GFP cell-to-cell diffusion (Fig 3E). Detailed analysis of REM1.3 phosphorylation mutants demonstrated that the phosphomimetic mutant recapitulated REM1.3 activity towards PD-aperture regulation, while the phosphodead mutant did not (Fig 3E).

Altogether, these results provide strong evidence that REM1.3's phosphorylation state at the evolutionarily conserved positions of S74, T86 and S91 is linked to its function in controlling viral infection and PD conductance.

REM1.3 phospho-status modulates its dynamic lateral segregation in the PM and PD sub-compartments

Both REM1.3 phosphomimetic and phosphodead mutants maintained PM localization, similarly to wild-type REM1.3, when transiently expressed in fusion with YFP in *N. benthamiana* (S4B Fig). Upon PVX infection we observed a modulation of REM1.3 PD-association and PM dynamics (Fig 1), linked to REM1.3 phosphorylation (Fig 2) that is required for REM1.3 function against PVX infection (Fig 3). We then asked whether different REM1.3 phospho-statuses might regulate its lateral organization at the PM and PD compartments in the absence of PVX. We examined the enrichment of REM1.3 YFP-tagged phosphomutants at the PD pit fields, previously calculated by the PD index (S1 Fig) and found that similarly to YFP-REM1.3, none

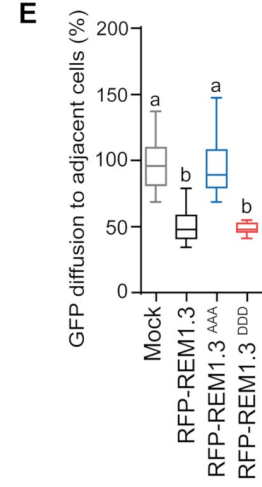
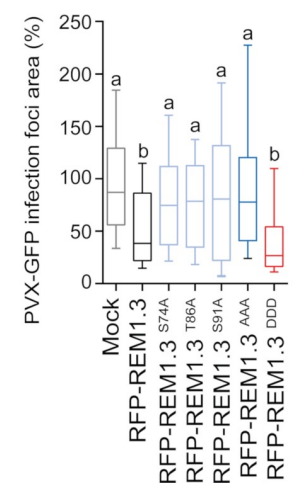
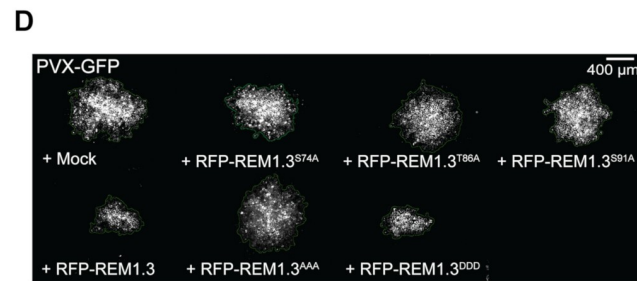
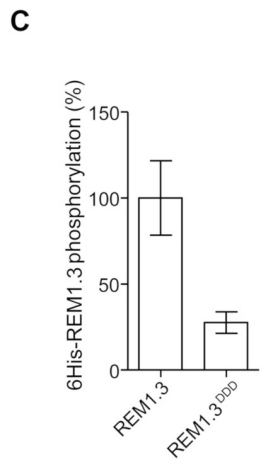
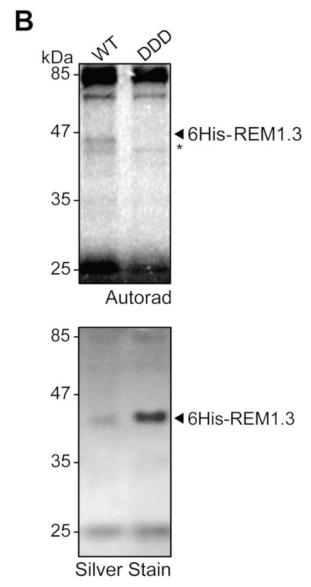
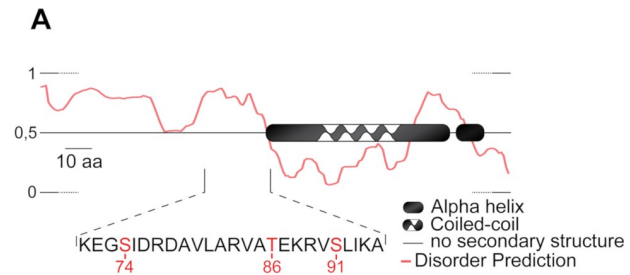


Fig 3. Mutational analysis reveals three critical phospho-residues required for REM1.3 regulation of PVX-GFP propagation and PD conductance. (A) *In silico* analysis of REM1.3 protein sequence. Prediction of putative phosphorylation sites was performed by Diphos, DEPP and NETPHOS coupled with published MS data. Predictions highlight three residues S74, T86 and S91 with high probability to be phosphorylated. Disordered prediction was performed by pDONR VL XT. Numbers indicate amino acid position. (B) *In vitro* kinase assay on recombinant affinity purified 6His-REM1.3 or 6His-REM1.3DDD by incubation with [γ - 33 P]-ATP and microsomal extracts of PVX-infected *N. benthamiana* leaves, as described in Fig 2. Phosphorylated proteins were detected by autoradiography and total proteins by silver staining. Asterisk * indicates phosphorylation of a *N. benthamiana* protein of close molecular weight not detected by silver staining. (C) Graph represents the relative quantifications from 4 independent reactions, using WT signal as a reference. (D) *Left*, Representative epifluorescence microscopy images of PVX-GFP infection foci on *N. benthamiana* leaf epidermal cells at 5 DAI. Graph represents the mean relative PVX-GFP foci area in cells transiently expressing RFP alone, wild-type RFP-REM1.3 or carrying single serine/threonine mutations to alanine. Co-infiltration of PVX-GFP with an empty *A. tumefaciens* strain served as mock control. Approximately 160 foci per condition from 3 independent biological repeats were measured. Letters indicate significant differences revealed by Dunn's multiple comparisons test $p < 0.001$. *Right*, Graph represents the mean relative PVX-GFP foci area in cells transiently expressing wild-type RFP-REM1.3 or triple RFP-REM1.3 phosphodead and phosphomimetic mutants compared to mock control (co-infiltration of PVX-GFP with an empty *A. tumefaciens* strain). Approximately 250 foci per condition from 5 independent biological repeats were measured. Letters indicate significant differences revealed by Dunn's multiple comparisons test $p < 0.001$. Epifluorescence microscopy images show representative PVX-GFP infection foci on *N. benthamiana* leaf epidermal cells at 5 DAI. (E) GFP diffusion to neighbor cells was estimated by epifluorescence microscopy at 5 DAI in *N. benthamiana* cells transiently expressing RFP-REM1.3 or phosphomutants. Measurements from 3 independent biological repeats were normalized to mock control (co-infiltration with an empty *A. tumefaciens* strain). Letters indicate significant differences determined by Dunn's multiple comparisons test $p < 0.001$.

<https://doi.org/10.1371/journal.ppat.1007378.g003>

of the phosphomutants appeared enriched at the pit field level (Fig 4A and 4C). The phosphodead mutant appeared statistically more excluded than YFP-REM1.3, whereas the phosphomimetic mutant displayed an increase of its PD index (Fig 4C), reminiscent of the REM1.3 localization phenotype under PVX infection (Fig 1A and 1B). Importantly, REM1.3 phosphomutants' association with PD was directly correlated with callose content at PD (Fig 4B). These observations reinforced the hypothesis that REM1.3-mediated increase of callose levels at PD is associated with a dynamic and phosphorylation-dependent redistribution of REM1.3 to the PD surroundings.

We next used spt-PALM VAEM to characterize the localization and mobility behaviour of the EOS-REM1.3 phosphomutants in the PM plane. The analysis of reconstructed trajectories and corresponding super-resolved localization maps indicated slight modifications of lateral mobility behavior between the phosphomutants (Fig 4D and 4E). Quantification of the diffusion coefficient values (D) extracted for each individual molecule revealed that EOS-REM1.3^{AAA} displayed a more immobile behavior than EOS-REM1.3^{DDD} and EOS-REM1.3. Consistently, EOS-REM1.3^{DDD} exhibited a higher mobility illustrated by higher diffusion coefficient and mean square displacement values (Fig 4D and 4E). Analysis of the supra-molecular organization of the phosphomutants by Voronoï tessellation (Fig 4F) firstly showed that all mutants displayed similar nanodomain size and localization density compared to EOS-REM1.3WT. Compared to EOS-REM1.3^{AAA}, the EOS-REM1.3^{DDD} nanodomains occupied a smaller area of the total PM and their density in the PM plane appeared slightly reduced (Fig 4F and 4G). A higher number of nanodomains were formed with the EOS-REM1.3^{AAA} mutant. Hence, the phosphomimetic mutations favor a less confined and a more dynamic localization pattern of REM1.3 at the PM, reminiscent to the phenotype of EOS-REM1.3WT in the context of PVX infection (Fig 1C and 1D).

These results suggest that differential REM1.3 phosphorylation is involved in regulating REM1.3 mobility and PM domain organization and support the hypothesis that REM1.3 phosphorylation on S74, T86 and S91 reflects an 'active form' of the protein necessary for REM1.3-mediated defense signaling.

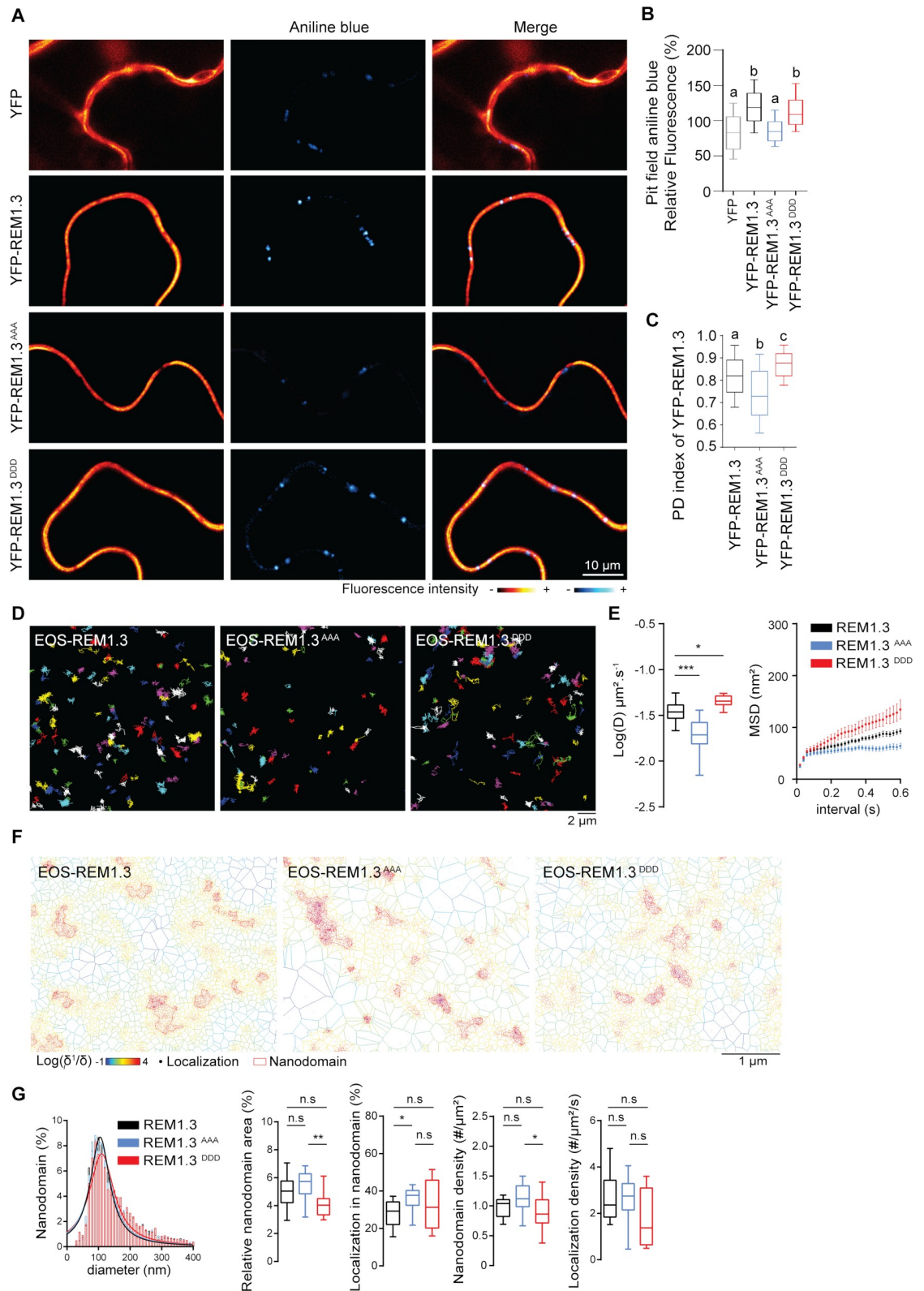


Fig 4. REM1.3's dynamic localization in PD and PM nanodomains is regulated by its phospho-status. (A) Representative confocal images showing aniline blue staining of callose deposition at the PD pitfields in *N. benthamiana* leaf epidermal cells transiently expressing YFP-REM1.3 or phosphomutants. Color-coding indicates fluorescence intensity. (B) Graphs show aniline

blue fluorescence intensities in cells transiently expressing YFP-REM1.3 and phosphomutants relative to control cells expressing YFP alone. Three independent biological experiments were performed and at least 15 cells per condition and per experiment were analyzed. Letter indicate significant differences revealed by Dunn's multiple comparisons test $p < 0.001$. (C) PD index of YFP-REM1.3 phosphomutants was calculated as described in S1 Fig. Graphs present quantifications from 3 independent biological experiments. Letter indicate significant differences revealed by Dunn's multiple comparisons test $p < 0.002$. (D) Super-resolved trajectories (illustrated by different colours) of transiently expressed EOS-REM1.3, and phosphomutants, transiently expressed in *N. benthamiana* cells, observed by spt-PALM. Scale bars, 2 μm . (E) Distribution of diffusion coefficients (D) represented as $\log(D)$ of the different fusion proteins. Mean Square Displacement (MSD) over time for the global trajectories of each EOS-REM1.3 construct followed during at least 600ms. 27 cells for EOS-REM1.3, 15 cells for EOS-REM1.3AAA and 17 cells for EOS-REM1.3DDD were analyzed in 3 independent experiments. Statistical analysis was performed by Mann-Whitney test * $p < 0.05$ ** $p < 0.01$. (F) Live PALM analysis of EOS-REM1.3 phosphomutants by tessellation-based automatic segmentation of super-resolution images. (G) Computation of EOS-REM1.3 and phosphomutants single molecule organization features based on tessellation-based automatic segmentation images. For REM1.3 and phosphomutants nanodomain size distribution and the Gaussian fits are indicated. Total nanodomain area is expressed as percentage of the total PM surface. Percentage of EOS-REM1.3 molecules localizing into nanodomains, relative to all molecules observed. Localization density refers to the number of molecules observed per μm^2 per second. Statistics were performed on at least 13 data sets per condition extracted from 3 independent experiments. Statistical differences determined by Mann-Whitney test * $p < 0.05$, ** $p < 0.01$.

<https://doi.org/10.1371/journal.ppat.1007378.g004>

AtCPK3 phosphorylates REM1.3

To gain more insights into the signaling processes leading to REM1.3 phosphorylation, we aimed to biochemically characterize the kinase(s) involved in the phosphorylation of REM1.3. Previous evidence suggested that the kinase(s) phosphorylating REM1.3 are membrane-associated (Fig 2) [38]. We therefore biochemically analyzed the localization of the kinase(s) phosphorylating REM1.3. Plant material from healthy and PVX-GFP-infected leaves was cell-fractionated to obtain crude extracts, soluble and microsomal fractions [59] to perform *in vitro* kinase assays on REM1.3N. Analysis confirmed a maximal kinase activity in purified microsomes (Figs 5A and 2A). Since a kinase in close proximity with its substrate would enhance reaction kinetics [60] and signal fidelity [61], and given that REM1.3 is enriched in detergent-resistant membranes (DRM) [8], we investigated whether the kinase activity towards 6His-REM1.3 is enriched in this biochemical fraction. We included "control PM" (C-PM) preparations, submitted to discontinuous sucrose gradients but in the absence of Triton-X100 treatments [62]. *In vitro* kinase assays on 6His-REM1.3N showed that the kinase activity in C-PM was 5 times inferior than in freshly purified PM not submitted to the sucrose gradient, suggesting that the kinase is not stable during the overnight purification procedure. Only half of the specific activity of the kinase was found in DRMs compared to the C-PM fraction, indicating that the kinase(s) phosphorylating REM1.3 is (are) only partially located in the DRM fraction (Fig 5B).

To gain more information concerning the biochemical characteristics of the kinase phosphorylating REM1.3, we analyzed its activity in the presence of known inhibitors. We firstly tested staurosporine, [63, 64] a general inhibitor that prevents ATP binding to kinases. We found an inhibition of REM1.3 phosphorylation starting at very low concentrations (30 nM) (S6A Fig). We further tested the effect of poly-L-lysine, described to stimulate the activity of the CK2 kinases and inhibit several CDPK kinases [65, 66]. No significant differences on REM1.3 phosphorylation levels were observed under increasing concentrations of poly-L-lysine (S6B Fig). The addition of the wide range of Ser/Thr phosphatases inhibitor β -glycerophosphate (BGP) [66] to the reaction mix did not alter the levels of phosphorylated 6His-REM1.3, indicating that the observed data was due to the activation of kinase activity by PVX rather than by inhibition of phosphatases (S6B Fig). Competition assays in the presence of cold AMP and GTP showed that only cold ATP even at 2 mM caused 20-fold depletion in [γ - ^{33}P] incorporation, suggesting that ATP is the major phosphoryl-donor for the kinase (S6B Fig). Addition in the reaction mix of 0,2 mM of EGTA, a chelator of Ca^{2+} , strongly inhibited the kinase activity suggesting that the kinase(s) phosphorylating REM1.3 in healthy leaves is

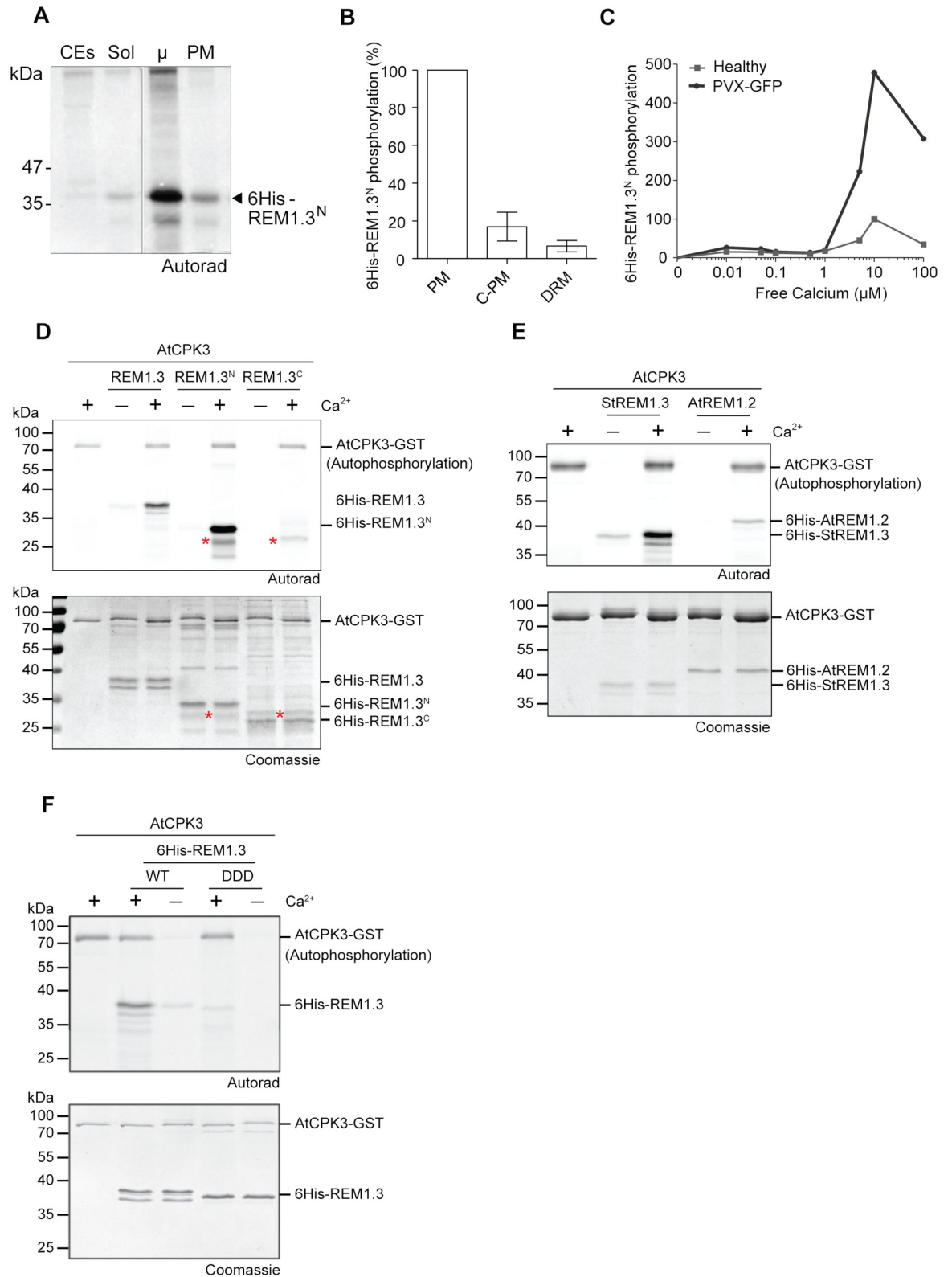


Fig 5. AtCPK3 phosphorylates REM1.3 in a calcium-dependent manner. (A, B) *In vitro* phosphorylation of purified 6His:REM1.3^N by kinase(s) from different cellular fractions of *N. benthamiana* leaves, CEs, leaf crude extracts; Sol, Soluble fraction; μ , microsomal fraction; PM, Plasma Membrane; C-PM: "Control-PM" is PM fraction not treated by TX100, but submitted to sucrose gradient; DRM, Detergent

resistant membranes [62]. The graph represents the relative quantification of 3 independent experiments normalized to the activity in the PM fraction +/- SEM. (C) Quantification of the calcium dose response of kinase activity on 6His-REM1.3^N phosphorylation by *N. benthamiana* microsomal extracts from healthy and PVX infected leaves. (D, E, F) Autoradiography gels show *in vitro* phosphorylation of 6His-REM1.3, 6His-REM1.3^N and 6His-REM1.3^C, 6His-REM1.3^{DDD} or 6His-AtREM1.2 by affinity purified GST-AtCPK3 in the presence or the absence of Ca²⁺. Bands corresponding to autophosphorylation of AtCPK3-GST and transphosphorylation of 6His-tagged group 1 REM variants are indicated. Gels were stained by coomassie blue to visualize protein loading. Asterisk* indicates a non-specific band present in both 6His-REM1.3^C and 6His-REM1.3^N preparation.

<https://doi.org/10.1371/journal.ppat.1007378.g005>

calcium sensitive (S6C Fig). Calcium is a conserved second messenger in signal transduction during biotic and abiotic stress. In plants, kinases harboring different calcium sensitivities can perceive calcium variations and translate them into downstream signaling activation [67, 68]. To determine whether the PVX-activated kinase phosphorylating REM1.3 is sensitive to calcium regulation, *in vitro* kinase assays from microsomes of healthy and PVX-infected *N. benthamiana* leaves were assayed in the presence of free calcium (Ca²⁺) concentrations ranging from 10 nM to 0,1 mM. Fig 5C shows that the kinase(s) displays a high sensitivity to calcium with an optimal activity in the presence of 10 μM of free Ca²⁺. At this concentration, a 5-fold increase of 6His-REM1.3^N phosphorylation was observed in PVX-infected leaves (Fig 5C). These experiments allowed us to narrow-down the kinase(s) phosphorylating REM1.3 after PVX infection to the group of membrane-bound Ca²⁺-dependent protein kinases [67].

Plants possess three main families of calcium-regulated kinases: calmodulin-binding kinases (CBKs), calcineurin B-like-interacting protein kinases (CIPKs) and calcium-dependent protein kinases (CPKs) [67]. CPKs have the unique feature of calcium sensing and responding activities in one single polypeptide, best characterized in the model plant *Arabidopsis* [67]. Based on the measured calcium dose response (Fig 5C), we correlated the kinase phosphorylating REM1.3 in *N. benthamiana* with homologs of Arabidopsis subgroup II AtCPKs [69], and we aimed to capitalize on the knowledge of Arabidopsis CPKs to test REM1.3 phosphorylation. Among the characterized members of subgroup II AtCPKs, we selected the Arabidopsis *AtCPK3* as a good candidate to test its putative role in REM1.3 phosphorylation, since previous proteomics studies in Arabidopsis have identified both *AtCPK3* and *AtREM1.3* as being enriched in PM, PD and DRM fractions [22, 70]. In addition, one study showed that *AtREM1.3* from microsomal fractions is phosphorylated *in vitro* by *AtCPK3* [71]. We therefore predicted that REM1.3 might share common functions with the evolutionarily conserved group 1b Arabidopsis REMs [32]. *AtREM1.2* and *AtREM1.3* are close homologs to REM1.3 and group 1 *N. benthamiana* REMs (NbREMs) in term of protein sequence [32, 36] and they conserved at least the S74 and S91 phosphorylation sites [39], [40, 57] (S5A Fig). Using super-resolution microscopy, Demir *et al.* showed that, when co-expressed in Arabidopsis leaves, REM1.3 and *AtREM1.3* co-localized in the same PM-nanodomains [72]. Importantly, transient expression of *AtREM1.2* and *AtREM1.3* in *N. benthamiana* epidermal cells impaired PVX-GFP cell-to-cell movement, as REM1.3 does (S5B Fig), strengthening the hypothesis that the function of group 1 REMs might be conserved between homologs in different plant species [36].

We assayed the *in vitro* phosphorylation activity of the affinity-purified AtCPK3-GST towards the 6His-REM1.3, the 6His-REM1.3^N and the 6His-REM1.3^C, as well as the homologous substrate 6His-AtREM1.2. Similar to our previous results (S3B and S3C Fig), AtCPK3-GST could phosphorylate strongly both 6His-REM1.3 and 6His-REM1.3^N, but not 6His-REM1.3^C (Fig 5D). In accordance with the effect of *AtREM1.2* in PVX-GFP propagation (S5B Fig), AtCPK3-GST can also phosphorylate 6His-AtREM1.2 (Fig 5E). Addition of Ca²⁺ is essential for a strong kinase activity as shown by both kinase auto-phosphorylation and transphosphorylation (Fig 5D and 5E). AtCPK3-GST specifically phosphorylated S74, T86 and S91

residues of REM1.3, since the phosphorylation was abolished in the phosphomimetic mutant 6His-REM1.3^{DDD} (Fig 5F).

These results suggest that AtCPK3 is a good candidate for group 1b REM phosphorylation and further support that the S74, T86, and S91 are the phosphorylation sites of REM1.3 (Figs 3A and 5E).

AtCPK3 interacts with group 1b REMs and restricts PVX propagation in a REM-dependent manner

CPKs harbor a variable N-terminal domain, a Ser/Thr kinase domain, an auto-inhibitory junction region and a regulatory calmodulin-like domain. The calmodulin-like domain contains four EF-hand binding motifs that determine the sensitivity of each kinase to calcium [73, 74]. To investigate the role of AtCPK3 in REM-dependent signalling, we generated AtCPK3 mutants presenting altered kinase activities. Deletion of the inhibitory junction region and the regulatory calmodulin-like domain in CPKs creates a constitutive active kinase while mutation of the aspartic acid residue in the catalytic center 'DLK' motif of the kinase domain to an alanine (D202A) creates a catalytically inactive or 'dead' kinase [67] (Fig 6A). We generated AtCPK3 full-length (AtCPK3), constitutive active (AtCPK3CA, residues 1–342) and kinase-dead (AtCPK3CAD202A) constructs for transient protein expression (Fig 6A). We evaluated their catalytic activities by expressing them transiently in Arabidopsis mesophyll protoplasts and performing immunoprecipitation coupled to kinase assays using 6His-REM1.3 and histone as a generic substrate [67]. Autoradiography confirmed that *in vivo* purified AtCPK3-CA-HA could trans-phosphorylate both 6His-REM1.3 and histone without the addition of calcium, while the point mutation D202A drastically abolished kinase activity (S7 Fig).

We next examined the sub-cellular localization of both *AtCPK3* and *AtCPK3CA* fused to YFP and found that both proteins disclosed a partial association with the PM, which was further confirmed by their presence, after cell fractionation, in the microsomal fraction at the expected molecular weight (Fig 6B) in good agreement with [71]. We further used *AtCPK3CA* to test the interaction with group 1b REMs. Bimolecular Fluorescence Complementation (BiFC) experiments showed that *AtCPK3CA* and REM1.3, REM1.3^{AAA} and REM1.3^{DDD} interact together at the level of the PM *in planta*. Importantly, we also confirmed the interaction of *AtCPK3CA* with homologous *AtREM1.2* and *AtREM1.3* (Fig 6C). REM1.3/REM1.3 interaction was used as a positive control, and *AtCPK3CA* /*AtCPK3CA* as a negative control.

We finally aimed to functionally characterize the *AtCPK3*- and REM1.3-mediated signaling in the context of PVX infection. Transient over-expression of *AtCPK3*-RFP alone induces a reduction of PVX-GFP infection foci suggesting that *AtCPK3* is indeed important for antiviral responses in plant cells (Fig 6D). Expression of the constitutively-active *AtCPK3CA*-RFP had a stronger effect on PVX-GFP spreading and to a similar degree with the over-expression of REM1.3 alone (Fig 6D). *AtCPK3*'s function towards PVX movement was observed to be mediated by its kinase activity, as the expression of the catalytically inactive mutant *AtCPK3CA*^{D202A} had no effect on PVX-GFP propagation (Fig 6D).

This raised the question whether the effect of *AtCPK3CA* on PVX propagation was REM-dependent. To tackle this question, we stably transformed *N. benthamiana* plants with a hairpin construct, to induce post-transcriptional gene silencing, which resulted in lowering RNA and protein expression of group 1 endogenous NbREMs (S8A and S8B Fig). Consistent with previous studies [8], silencing of group 1 REM correlates with an increase of PVX-GFP cell-to-cell movement in inoculated leaves (S8C Fig). No difference was observed by ELISA when measuring PVX accumulation in systemic leaves (S8D Fig). Importantly, PVX assays demonstrated that *AtCPK3CA* ability to restrict PVX movement was impaired in two independent *N.*

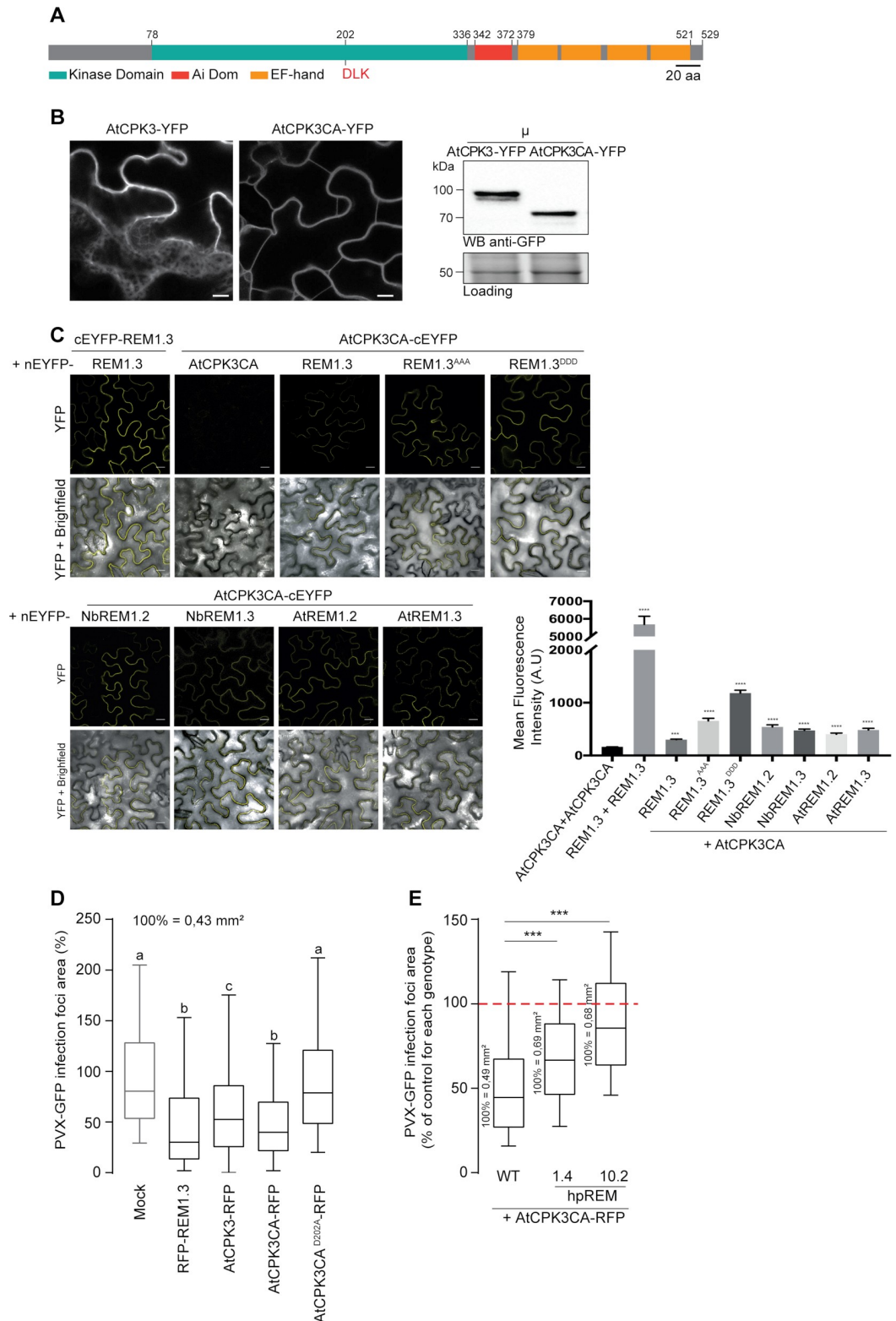


Fig 6. AtCPK3 physically interacts *in vivo* with group 1b REMs and impairs PVX cell-to-cell movement in a REM-dependent manner. (A) Primary sequence of AtCPK3. EF-hands are helix E-loop-helix F structural domains able to bind calcium. Ai: Autoinhibitory domain. The position of the DLK motif (Aspartic acid-Leucine-Lysine) at the catalytic domain conserved in all CPKs is indicated. (B) Confocal images showing AtCPK3-YFP and AtCPK3CA-YFP localization in *N*.

benthamiana epidermal cells. Scale bar shows 10 μm . Western blot against GFP showing AtCPK3-YFP and AtCPK3CA-YFP expression in the microsomal fraction (μ) of *N. benthamiana* leaves. (C) *In planta* Bimolecular Fluorescence Complementation (BiFC) analysis showing interaction of AtCPK3 with Group 1 REMs. REM1.3-YFPN/REM1.3-YFPC was used as a positive control, and AtCPK3CA-nYFP/ AtCPK3CA-cYFP as a negative control. Mean fluorescence intensity at the cell boundary level was recorded using ImageJ. Statistical differences were determined by Mann-Whitney test compared to AtCPK3CA +AtCPK3CA.*** $p = 0.0002$, **** $p < 0.0001$. All scale bars indicate 20 μm . (D) PVX-GFP spreading in *N. benthamiana* cells expressing RFP-REM1.3 or AtCPK3FL-RFP, AtCPK3CA-RFP, AtCPK3CAD202A-RFP. Graph represents the area of PVX-GFP infection foci relative to the mock control (co-infiltration of PVX-GFP with empty *A. tumefaciens*). At least 200 PVX-GFP infection foci from at least 3 independent repeats were imaged at 5DAI. Letters indicate significant differences revealed by Dunn's multiple comparisons test $p < 0.001$. (E) Effect of AtCPK3CA on PVX-GFP cell-to-cell movement in WT *N. benthamiana* or in transgenic lines constitutively expressing hairpin REM (hpREM) constructs. At least 200 PVX-GFP infection foci from at least 3 independent repeats were imaged at 5DAI. For each *N. benthamiana* line the effect of AtCPK3CA is expressed as a percentage of the corresponding mock control (empty *Agrobacteria*). Absolute values of the average foci area for each mock control are indicated.

<https://doi.org/10.1371/journal.ppat.1007378.g006>

benthamiana lines underexpressing group 1 REM levels, (namely lines 1.4 and 10.2 with expression levels decreased respectively by 2 and 20 times) (Fig 6E), indicating that REMs might be the direct substrate of CPK3 *in vivo*.

Altogether, these data suggest that CPK3 and group 1 REMs are major regulators involved in signaling and antiviral defense at the PM level.

Discussion

Protein phosphorylation is a ubiquitous and specific mechanism of cell communication [75]. The addition of a phosphate group on one or more critical residues of a given protein can induce important conformational changes that affect energetically favorable interactions and may lead to changes in its interacting network, localization, abundance and may influence the activity of protein signaling pools [76]. Although, since the initial discovery of REM1.3 in 1989, accumulating evidence suggests that the functions of REM proteins are regulated by protein phosphorylation [38–40]. The biological significance of this phosphorylation remained unclear to this date. REM proteins were among the first plant proteins described which supported the notion of PM sub-compartmentalization to functional protein-lipid nanodomains [8, 11, 77], also named membrane rafts [3, 4, 21]. In the present paper, we used REM1.3 and PVX as an experimental system to study the role of protein phosphorylation and membrane dynamics in the context of stress response.

REM1.3 functions likely involve distinct PM compartments during plant PVX-sensing

Understanding how plants defend themselves against viruses remains a challenging field. The canonical plant immune response against viruses is mainly represented by the mechanism of RNA silencing [78, 79], while additional mechanisms of plant antiviral defense involve hormonal signaling, protein degradation, suppression of protein synthesis and metabolic regulation [51, 78, 80]. Antiviral defense presents similarities to the immune response against microbes [81–83]. Compelling evidence suggests that cell-surface as well as intracellular plant immune receptors recognize viral elicitors [55, 84–89]. An additional number of host cell components have been shown genetically to affect viral replication or cell-to-cell movement [8, 90], indicating that more sophisticated plant defense mechanisms against viruses may exist.

For instance, manipulation of REM levels in transgenic *Solanaceae* suggested that REM is as a positive regulator of defense against the PVX by affecting viral cell-to-cell movement [8, 14, 36]. We recently showed that REM1.3 does not interfere with the suppressor ability of PVX movement protein TGBp1, but specifically affects its gating ability [33]. Group 1 REMs could

be a target for viruses (and other pathogens) to circumvent infection as illustrated by the case of *Rice Stripe Virus* that targets NbREM1 for degradation by 26S proteasome [91]. Nevertheless, in this study we show that REM1.3 protein levels are not altered during PVX infection (S2C and S2D Fig).

In this paper, we provide supporting mechanistic evidence that REM1.3 regulates the levels of callose accumulation at PD pit fields during PVX infection (Fig 1). Whether this function is mediated by a direct interaction with callose synthase/glucanase complexes remains however still unknown. Surprisingly, we found that REM1.3 is not dramatically recruited to PD pit fields, although its PD index is slightly increased after PVX infection (Fig 1). This suggests that association of a sub-fraction of the REM1.3 to the PD-PM region may be sufficient to increase callose accumulation, although we cannot rule out the possibility that REM1.3 may regulate PD permeability *via* a more indirect mechanism. The spt-PALM VAEM microscopy data supports an increase of protein mobility and redistribution to distinct domains during PVX infection (Fig 1). These findings indicate the existence of a mechanism that operates at specific REM1.3-associated PM nanodomains, capable of regulating PD permeability (Fig 1). The dynamic partitioning between PM nanodomains and PD pit fields needs to be further studied.

Plant PVX-sensing induces the activation of a calcium-dependent protein kinase

Since various studies have reported REM phosphorylation during plant-microbe interactions [16, 17, 39, 40], we set out to address which kinase phosphorylates REM and whether REM1.3 phosphorylation plays a role in REM-mediated anti-viral defense. Indeed, our experimental findings show that plant PVX sensing induces the activation of a membrane-bound calcium-dependent protein kinase that in turn phosphorylates REM1.3 (Fig 2, Fig 5). Importantly, we show that the kinase able to phosphorylate REM1.3 is activated specifically by the expression of two PVX proteins, namely CP and TGBp1. Deciphering the exact mechanisms allowing the molecular recognition of those PVX components will be a crucial step toward understanding REM-mediated anti-viral defense. Intriguingly, the finding that the presence of *Agrobacterium* also induces REM1.3 phosphorylation (Fig 2G) is in agreement with previous reports suggesting phosphorylation of REMs under bacterial infection [39, 40] and suggests that phosphorylation should be also a way to regulate -yet unknown functions- of REM1.3 in bacterial defense.

Genetic studies have established that different CPKs comprise critical plant signaling hubs by sensing and translating pathogen-induced changes of calcium concentrations [67, 68]. Biochemical characterization of the kinase phosphorylating 6His-REM1.3 showed that its strong sensitivity to calcium (Fig 5C) corresponds to homologs of phylogenetic subgroup II CPKs from *Arabidopsis* [67]. CPK3 is a prominent member of subgroup II, shown to function in stomatal ABA signaling [92], in salt stress response [71, 93] and in a defense response against an herbivore [94]. Interestingly, it was suggested that *AtREM1.3* from taxonomical group 1 of REMs could be a substrate for *AtCPK3* in response to salt stress [71]. Here we show that *AtCPK3* can interact *in vivo* with group 1 REM (Fig 6C) and that *AtCPK3* phosphorylates group 1 REM in an *in vitro* kinase assay (Fig 5D). Transient overexpression of *AtCPK3* in *N. benthamiana* resulted in a reduction of PVX propagation in a REM-dependent manner, providing compelling evidence that CPK3 together with REM contribute to the plant antiviral immunity. This is the first report demonstrating the participation of CPKs in plant basal immunity against viruses.

Although [95] reports that there is no calcium signal during early recognition of PVX, the activation of CPKs by PVX supports the notion that calcium might be involved in some other late steps of plant-virus interaction like the control of intercellular connectivity. These changes

in calcium concentrations in the cell are sensed by the CPKs and translated via the phosphorylation of REM and/or other unknown downstream components. In *Nicotiana tabacum* calmodulin isoforms are critical for the plant resistance against Tobacco Mosaic Virus and Cucumber Mosaic Virus, further illustrating the existence of virus-specific patterns of calcium signals [96, 97]. More work is needed to identify the CPK family members participating to the response and also the nature and specificity of those PVX-induced calcium changes.

Phosphorylation regulates group 1 REM's function during PVX cell-to-cell movement

AtCPK3 specifically phosphorylated REM1.3 at its N-terminal domain (residues 1–116), a domain displaying a mostly intrinsically disordered secondary structure (Figs 3A and 5). *In silico* analysis followed by a mutagenesis approach coupled with *in vitro* kinase assays revealed three major putative phosphorylation sites for REM1.3, namely S74, T86 and S91 on REM1.3. The *in vitro* phosphorylation of REM1.3 (Figs 3A and 5E) is almost totally lost when S74, T86 and S91 are mutated to non-phosphorylatable residues, confirming these residues as major REM1.3 phosphorylation sites. Individual phospho-null mutations at those sites impaired REM1.3 ability to restrict PVX cell-to-cell movement to various extent (Fig 3D). The triple phospho-null mutant, YFP-REM1.3^{AAA} totally obliterated REM1.3's capability to restrict PVX cell-to-cell movement (Fig 3D) and to regulate PD permeability (Fig 3E). Reciprocally, REM1.3 triple phosphomimetic mutant, RFP-REM1.3^{DDD} appeared fully functional (Fig 3E and 3F). These results strongly support the functional involvement of single or combined phosphorylation in the N-terminal domain of S74, T86 and S91 to establish REM's function in the context of PVX infection. This is in contrast with LjSYMREM1 from *Lotus japonicus* which was shown to be phosphorylated at its C-terminal domain *in vitro* by SYMRK [16]. Despite the fact that phosphorylation of REM proteins has been widely reported [16, 17, 39, 40, 57], this work firstly describes an associated role of REM-induced phosphorylation with its function.

Toward the understanding of REMORIN function

Our finding that overexpression of *AtREM1.2* and *AtREM1.3* also restricts PVX-GFP cell-to-cell movement (S5B Fig) suggests that REM phosphorylation and its associated functions might be conserved for some REMs of taxonomic group 1b. In good agreement, *AtREM1.2* and *AtREM1.3* localize to the same PM nanodomains [72] and maintain conserved phosphorylation sites with REM1.3 (S5A Fig). By contrast, *AtREM4.1* from subgroup 4, presenting a different N-terminal domain and different expected phosphorylation profile has an opposite effect against geminiviral propagation by promoting susceptibility to *Beet curly top virus* and *Beet severe curly top virus* [17, 57]. This further argues that REMs might be phosphorylated by diverse families of kinases in order to respond to different stimuli [57].

Overexpression of REM1.3 restricts TMV propagation (S4A Fig), and additionally modulates the movement proteins from different virus genera [33, 91]. These findings suggest that the initial hypothesis that REM1.3 causes the sequestration of the PVX virions at the PD [8] might not hold true, but rather that REM1.3 might have a more general role in plant stress and PD regulation (Figs 1 and 3). Interestingly, REM1.3 promotes susceptibility to *Phytophthora infestans* in *N. benthamiana* and localizes exclusively to the PM and the extrahaustorial membrane around non-callosic haustoria [42]. The exact role of REM1.3 as a common regulator of different signaling pathways and its role in PD permeability regulation remains to be determined.

It has been speculated that phosphorylation in intrinsically disorder regions of proteins may act as a molecular switch and confer potential protein-protein interaction plasticity [76, 98]. The intrinsically disordered REM1.3 N-terminal domain exhibits the most sequence variability in REM proteins, presumably conferring signaling specificity [32, 57]. Phosphorylation of *AtREM1.3*'s N-terminal domain could stabilize coil-coiled-associated protein trimerization and protein-protein interactions [57]. Phosphorylated REM1.3 seems to be further targeted to PD-PM to trigger callose deposition. In good agreement, we found that the mobility in the PM of REM1.3 changed depending on its phospho-status (Fig 4). The triple phosphomimetic mutant exhibited a less confined and more mobile behavior at the PM, reminiscent of the WT protein in the context of PVX infection (Fig 4D). Similarly to the role of 14.3.3 proteins in plants [99], REM1.3 could act as a scaffolding protein, interacting with multiple members of a signaling pathway and tethering them into complexes to specific areas of the membrane. Hence, REM1.3 phosphorylation could act as a regulatory switch of protein conformations that would modulate REM1.3 specific interaction patterns and transient signalosomes at the PM. The triple phosphomimetic REM mutant might reflect a 'functionally active' form that constitutes REM-guided signalosomes against PVX-infection at the PM and should be exploited in future studies. The study of the phosphorylation-dependent interactions of REM1.3 (and related phosphocode) in regard to the modulation of REM1.3 PM dynamics and molecular function is the topic for future studies.

Materials and methods

Plant material

Nicotiana benthamiana plants were cultivated in controlled conditions (16 h photoperiod, 25 °C). Proteins were transiently expressed via *Agrobacterium tumefaciens*-mediated transformation for virus and PD functional assays as in [14, 33] or for the localization experiments as described in the appendix. For subcellular localization studies and protein extractions, plants were analyzed 2 or at 4 days after inoculation (DAI) in the phosphorylation assays. Imaging for PVX-GFP spreading assays and plasmodesmata GFP-diffusion experiments were done at 5 DAI. PVX inoculation for test ELISA was performed at 4-week-old *N. benthamiana* plants. Details on molecular cloning and protein work, transgenic lines generation are described in the Appendix.

Cloning and molecular constructs

All vectors constructs were generated using classical Gateway cloning strategies (www.lifetechnologies.com), pDONR211 and pDONR207 as entry vectors, and pK7WGY2, pK7YWG2, pK7WGR2, pK7RWG2, and pGWB14 and pGWB15 as destination vectors [100]. The REM1.31–116, REM1.3117–198 and REM1.3 single S74A, T86A and S91A and triple S74/T86/S91AAA and S74/T86/S91DDD mutants were synthesized in a pUC57 vector (including the AttB sites) by Genscript (<http://www.genscript.com/>) or GENEWIZ (<http://www.genewiz.com/>) and next cloned to Gateway destination vectors. AtCPK3D202A mutant was generated by site-directed mutagenesis as previously described [101] with minor modifications. For BiFC experiments, the genes of interest were cloned into pSITE-BIFC- C1nec, -C1cec, -N1nen, and -N1cen destination vectors [102]. To map the dynamics of single molecules with sptPALM, REM1.3 and phosphomutants were cloned in fusion with EOS in the gateway compatible vector pUBN-Dest::EOS [103]. EOS protein has been widely use for single molecule localization microscopy in mammals, bacteria, and plant cells. It corresponds to the name of a fluorescent protein from the stony coral *Lobophyllia hemprichii* which peculiarity resides in its photoconvertability. The energy of UV light can break the core polypeptidic

chain of EOS fluorescent protein inducing changes in EOS spectral fluorescence properties. Due to the stochasticity of EOS photoconversion at low UV radiation (space and number of events/sec can be controlled by modulating UV laser power), single molecules can be converted, localized and tracked.

Generation of transgenic stable hairpin REM and 35S::GFP-REM1.3 *N. benthamiana* lines

Leaf discs were cut from *N. benthamiana* leaves, transferred on petri plates containing culture medium (complete Murashige and Skoog medium (MS) supplemented with 30g/L saccharose, pH 5,8; phytoagar HP696 (Kalys) 5,5 g/L and the hormones: AIA 0,1 mg/L, BAP 2 mg/L) and incubated for 48 h in the growth room (16 h photoperiod, 30 $\mu\text{mol photons.m}^{-2}.\text{s}^{-1}$, 23 °C). For the transformation, the *N. benthamiana* plants disk leaves were incubated with the *Agrobacterium* cultures (GV3101 strain) carrying the plasmid of interest for 20 min. The leaf samples were next placed on plates with the complete medium previously described. 48 hours later, the leaf fragments were washed 3 times with sterile water (with 0,1% Tween20). The leaf fragments were next washed with MS complete medium supplemented with Timentin (300 $\mu\text{g/mL}$). The leaves were next placed on plates with regeneration medium (MS culture medium, as previously described, supplemented with 300 mg/L of timentin and 150 mg/l of kanamycin). The plates were next incubated in the growth room. The explants were transferred to fresh regeneration medium with a maximum periodicity of 7 days until the development of callus. The regenerated seedlings were transferred to a rooting medium (MS, sucrose 30 g/L, phytoagar 5,5 g/L, timentin 200 mg/L, kanamycin 150 mg/L). The regenerated plants (T0) were transferred to the greenhouse for growth and self-fertilization. Homozygous T2 lines carrying a single transgene insertion were selected by segregation analysis on selective Kanamycin media and used for physiological studies and phenotypic characterization. The expression of the GFP-REM1.3 or silencing levels of endogenous NbREMs was controlled by cytological, biochemical and expression analysis. Cytological analysis of the GFP-REM1.3 expression in all leaf cells was performed to avoid chimeric expression, see [S2A and S2B Fig](#).

Transient expression in *N. benthamiana*

Four-week-old *N. benthamiana* greenhouse plants grown at 22–24 °C were used for *Agrobacterium tumefaciens*-mediated transient expression. *A. tumefaciens* were pre-cultured at 28 °C overnight and used as inoculum for culture at initial OD_{600nm} of 0.15 in pre-warmed media. Cultures were grown until OD_{600nm} reached 0.6 to 0.8 values (3–5 h). Cultures were then centrifuged at 3,200 g for 5 min, pellet were washed twice, using water to the desired OD_{600nm}. Bacterial suspensions at OD_{600nm} of 0.2 and 0.1 were used for subcellular localization and Spt-PALM experiments, respectively. The bacterial suspensions were inoculated using a 1-mL syringe without a needle by gentle pressure through a <1mm-hole punched on the lower epidermal surface [104]. Transformed plants were incubated under normal growth conditions for 2 days at 22–24 °C. Transformed *N. benthamiana* leaves were analyzed 2–5 DAI depending on the experiment.

Viral spreading, GFP diffusion assays

PVX-GFP cell-to-cell movement experiments were performed as previously described [14, 36], with minor modifications. Briefly, *A. tumefaciens* strain GV3101 carrying the constructs tested were infiltrated at a final optical density at 600 nm (OD_{600nm}) = 0.2 together with the same strain carrying the plasmid pGr208, which expresses the PVX-GFP complementary DNA harboring GFP placed under the control of a Coat protein promoter, as well as the helper

plasmid pSoup [105] at final OD_{600nm} of 0.001. Viral spreading of PVX-GFP was visualized by epifluorescence microscopy (using GFP long pass filter on a Nikon Eclipse E800 with x4 objective coupled to a Coolsnap HQ2 camera) at 5 DAI and the area of at least 30 of PVX-GFP infection foci was measured using Fiji software (<http://www.fiji.sc/>) via a homemade macro or ImageJ. The expression levels of transiently expressed constructs were confirmed by Western blot. ELISA tests in systemic *N. benthamiana* leaves were performed similarly to [8] to follow the global virus accumulation. Briefly, GFP-REM1.3 or hpREM plants were mechanically inoculated with PVX, and viral accumulation in systemically invaded leaves (at 3 nodes above the inoculated leaf) was evaluated at 10 or 14 DAI with a specific anti-PVX coat protein antibody (Sediag). Five plants per line for GFP-REM1.3 and 8 for hpREM plants were tested per experiment. GFP diffusion at PD experiments was performed as previously described [33]. All the experiments were repeated at least three times.

Epidermal cells live imaging and quantification. Bimolecular Fluorescence Complementation

Live imaging was performed using a Leica SP5 confocal laser scanning microscopy system (Leica, Wetzlar, Germany) equipped with Argon, DPSS and He-Ne lasers and hybrid detectors. *N. benthamiana* leaf samples were gently transferred between a glass slide and a cover slip in a drop of water. YFP and mCitrine (cYFP) fluorescence were observed with similar settings (*i.e.*, excitation wavelengths of 488 nm and emission wavelengths of 490 to 550 nm). In order to obtain quantitative data, experiments were performed using strictly identical confocal acquisition parameters (*e.g.* laser power, gain, zoom factor, resolution, and emission wavelength reception), with detector settings optimized for low background and no pixel saturation. Pseudo-colored images were obtained using the “Red hot” look-up-table (LUT) of Fiji software (<http://www.fiji.sc/>). All quantifications were performed for at least 10 cells, at least two plants by condition with at least 3 independent replicates. BiFC images were taken 2 DAI by confocal microscopy (Zeiss LSM 880). Quantification of fluorescent intensities was performed by ImageJ, as described in [36].

Spt-PALM, single molecule localization and tracking

N. benthamiana epidermal cells were imaged at room temperature (RT). Samples of leaves of 2-week-old plants expressing EOS constructs were mounted between a glass slide and a cover slip in a drop of water to avoid dehydration. Acquisitions were done on an inverted motorized microscope Nikon Ti Eclipse (Nikon France S.A.S., Champigny-sur-Marne, France) equipped with a 100× oil-immersion PL-APO objective (NA = 1.49), a TIRF arm, a Perfect Focus System (PFS), allowing long acquisition in oblique illumination mode, and a sensitive Evolve EMCCD camera (Photometrics, Tucson, USA). Images acquisitions and processing were done as previously described [45].

Single molecule fluorescent spots were localized in each image frame and tracked over time using image processing techniques such as a combination of wavelet segmentation [106] and simulated annealing algorithms [107]. The software package used to extract quantitative data on protein localization and dynamics is custom written as a plug-in running within the MetaMorph software environment. This plugin is now property of Molecular devices company (<https://www.moleculardevices.com/sites/default/files/en/assets/product-brochures/dd/img/metamorph-super-resolution-software.pdf>).

Single molecule localization organization analysis, $\text{Log}(\delta 1/\delta)$ correspond to the ratio between the local molecule density to overall molecule density at the PM. After correction for artefacts due to multiple single-molecule localization (described in [36] and now presented in

material and methods section), we computed potential nanodomain by applying a threshold $\delta l_i > 2\delta N$, where δN is the average localization density at PM level and δl_i is the density in presumed protein-forming nanodomain, with a minimal area of 32 nm² and with at least 5 localizations per nanodomain.

SR-Tesseler software was used to produce Voronoï diagrams, and subsequently quantify molecule organization parameters as previously recommended [50]. Taking in account fluorophore photophysical parameters, localization accuracy and the first rank of local density of fluorescent molecules, correction for multiple detections occurring in a vicinity of space (w) and blinking tolerance time interval (t) are identified as the same molecule, merged together and replaced by a new detection at a location corresponding to their barycentre. Because first rank of local density of fluorescent molecules was below 0.5 mol/mm² (c.a ranking from 0.1 to 0.3 mol/mm²), we used a fixed search radius w of 48 nm as recommended [50]. To determine the correct time interval t , the photophysics of the fluorophore namely the off-time, number of blinks per molecule and on-time distributions are computed for each cell. For example, for a dataset composed of 618,502 localizations, the average number of blinks per molecule was 1.42, and the number of molecules after cleaning was 315,929. As a control, the number of emission bursts (439,331), counted with $t = 0$, divided by the average number of blinks per molecule (1.42) was only 2.15% different. After correction for artefacts due to multiple single-molecule localization, we computed potential cluster using a threshold $d l_i > 2d N$, where $d N$ is the average localization density at PM level and $d l_i$ is the density in presumed protein-forming nanocluster, with a minimal area of 32 nm² and with at least five localization by cluster.

Over the two independent experiments 54 446 single molecule trajectories have been observed (34 740 Mock / 19 706 PVX). We then computed single molecule mobility behavior (Diffusion coefficient and Mean square displacement) using trajectories of at least 8 time points (tracked for at least 0.16 s; representing 19495 trajectories in total, 12073 for Mock condition and 7422 for PVX condition).

***In silico* analysis of REM1.3 protein sequence**

Prediction of putative phosphorylation sites was performed by Diphos, DEPP and NETPHOS coupled with published data. Disordered domains were performed by pDONR VL XT.

***In vitro* REM1.3 phosphorylation assays**

6His-REM1.3 and mutant recombinant proteins were purified from bacteria using fast flow chelating sepharose resin (Amersham) according to manufacturer's instructions and as in [14]. For the *in vitro* REM1.3 phosphorylation assays about 2 µg of total plant extracts were incubated with 1 µg of affinity-purified 6His:REM1.3 protein variants for 10 minutes at room temperature and in a phosphorylation buffer (Tris-HCl 30mM, EDTA 5mM, MgCl₂ 15mM, DTT 1mM, Na₃VO₄ 2,5 mM, NaF 10 mM and 10 µCi/reaction ATP [γ -³³P]- (3000Ci/mmol, Perkinelmer). The buffer contained also 10–5 M of free Ca²⁺ which allows the detection of 6His-REM1.3 phosphorylation also in mock conditions. Gradual concentrations of free Ca²⁺ as in [108] were added for Fig 5C. Reactions were performed for 15 minutes in a volume of 25 µl. The reactions were stopped by the addition of 15 µl of 6x loading buffer. Proteins were separated by SDS-PAGE and phosphorylation status of REM1.3 was analysed by autoradiography using a phosphor-Imager and quantified by ImageQuant TL program.

***In vitro* CPK3 kinase assays**

CPK3-HA was transiently expressed in mesophyll protoplasts and immunopurified with anti-HA antibodies as performed in [109] while CPK3-GST recombinant protein was purified

from bacterial extracts as reported in [69]. For *in vitro* kinase assays, the tagged CPK was incubated with 0.5–1 μg histone or 6His-REM1.3 proteins in the following kinase reaction buffer (20 mM Tris HCl pH 7.5, 10 mM MgCl_2 , 1 mM DTT, 50 μM cold ATP, ATP [γ - ^{33}P] 2 μCi per reaction, 1 mM CaCl_2 or 5 mM EGTA) in a volume of 15 μL for 30 min at RT. The reaction was stopped with 5 μL 4X Laemmli buffer, then samples were heated at 95 $^\circ\text{C}$ for 3 min. Proteins samples were separated by SDS-PAGE on 12% acrylamide gel. After migration, the gel was dried before exposing against a phosphorScreen to reveal radioactivity on a Storm Imaging system (GE Healthcare). The gel was then rehydrated for Coomassie staining.

Protein work

SDS-PAGE, Western Blot analysis, protein extractions and recombinant protein purification were performed in *E. coli* as in [14]. Cell fractionation and extractions followed the established protocol from [59] and [62]. Anti-REM antibodies were previously described in [8].

Accession numbers

All relevant data are within the paper and its Supporting Information files are available from Arabidopsis Genome Initiative (<https://www.arabidopsis.org/index.jsp>), and GenBank/EMBL (<https://www.ncbi.nlm.nih.gov/genbank/>) databases under the accession numbers: *StREM1.3* (NP_001274989), *AtREM1.2* (At3g61260), *AtREM1.3* (At2g45820), *AtCPK3* (At4g23650).

Supporting information

S1 Fig. Callose quantification by aniline blue staining and PD index calculation. (A) Original sample image is an 8-bit, single-channel image.

(B) Masks of total Region Of Interest (ROI) objects before particle analysis were created using the following filters; background subtraction with a rolling ball radius as in [43]; “smooth” twice and an auto-local threshold Max Entropy dark, creating a black and white mask, used for particle detection.

(C) Overlay of outlines of the analyzed ROI (green; after particle analysis with particle size 3–100 pixel^2 circularity (0.3–1) exclude on edge) with the original image. Scale bar indicates 10 μm .

(D) Quantification of PD Index; after aniline blue labeled pit-field detection, YFP-REM1.3 fluorescence intensity was manually measured at pit-field level (ROI2) and surrounding PM (ROI1 and ROI3) using a circle of fixed area (0.18 μm^2). The PD index was then calculated as the ratio between YFP-REM1.3 pit-field fluorescence (ROI2) and the mean of YFP-REM1.3 fluorescence intensity at surrounding PM (ROI1+ROI3).

(TIF)

S2 Fig. Overexpression of GFP-REM1.3 results in reduced PVX accumulation in *N.*

benthamiana and REM1.3 protein levels are not affected by PVX infection. A. Top, Confocal image showing GFP-REM1.3 localisation in the PM in *N. benthamiana* lines Bottom, The GFP:REM1.3 expression in three independent transgenic lines #6, 7 and 16 was tested by Western blot against REM and showed that it contains at least three times the amount of endogenous *N. benthamiana* REM.

B. PVX infection assays in independent stably expressing GFP-REM1.3 and wild-type control *N. benthamiana* lines. Viral charge was assayed by test DAS-ELISA using antibodies to PVX coat protein on distal (3 nodes above inoculation) leaves at 14 DAI. Three independent experiments were performed with five plants for each transgenic line and non-transgenic (WT).

Error bars show SE, and significance is assessed by Dunnett’s multiple comparison test against

WT (*, $P < 0.1$; **, $P < 0.05$; ***, $P < 0.001$).

C, Western blot against REM1.3 was performed on total protein extracts from wild type *N. benthamiana* leaves infected by PVX-GFP at 0, 3, 5 and 7 DAI. Stain free loading is indicated below.

D, Confocal images showing PVX-GFP foci at the indicated DAI, tested in C. (TIF)

S3 Fig. Analysis of *in vitro* 6His-REM1.3 phosphorylation and viral proteins expression.

(A) Effect of the addition of ATP or AMP in *in vitro* phosphorylation assays of 6His-REM1.3 by kinase(s) in microsomal (μ) or PM extracts of *N. benthamiana* leaves developed by autoradiography.

(B) 6His-REM1.3^N and 6His-REM1.3 phosphorylation by healthy *N. benthamiana* leaf microsomal (μ) and plasma membrane (PM) extracts.

(C) 6His-REM1.3^N and 6His-REM1.3^C phosphorylation by kinase(s) in microsomal (μ) and soluble extracts.

(D) 6His-REM1.3 was differentially phosphorylated by leaf microsomal extracts expressing the indicated constructs *i.e.* PVX alone, PVX deleted for TGBp1 (PVX Δ TGBp1), 30K protein from Tobacco Mosaic Virus (TMV), PVX fused to GFP, and GFP alone at 4 DAI. See the rationale Fig 2E. Control of loading is shown after stain free procedure. In all phosphorylation experiments about 10 μ g of total protein extracts and 1 μ g of affinity purified 6His-REM1.3, REM1.3^N or REM1.3^C were loaded per lane.

(E) Controls of expression of fluorescently-tagged viral proteins, namely CP, TGBp1, TGBp2 used in Fig 2. (TIF)

S4 Fig. REM1.3 S74 T86 S91 phosphorylation is important to regulate Tobacco mosaic virus movement and REM1.3 phosphorylation mutants maintain PM localization.

(A) Representative epifluorescence microscopy images of Tobacco Mosaic Virus (TMV-GFP) infection foci in *N. benthamiana* leaf epidermal cells at 5 DAI. Graph represents the relative foci area of REM1.3 or phosphomutants (S74, T86 and S91 into Alanine, AAA or Aspartic Acid, DDD) compared to mock control (co-infiltration of PVX-GFP with an empty *A. tumefaciens* strain). About 78–128 foci per condition were measured in 2 independent biological repeats. Dunn's multiple comparison tests were applied for statistical analysis, $p < 0.001$.

(B) Confocal microscopy images of secant views of *N. benthamiana* epidermal cells expressing YFP-REM1.3, YFP-REM1.3AAA and YFP-REM1.3DDD at 2 DAI. Scale bar indicates 10 μ m. (TIF)

S5 Fig. Group 1b AtREMs and REM1.3 have similar behavior against PVX cell-to-cell movement in *N. benthamiana* epidermal cells. (A) Clustal alignments of protein sequences of group 1b REMORINs: *AtREM1.2*, *AtREM1.3*, *NbREM1.2*, *NbREM1.3* and REM1.3 (*StREM1.3*). Blue color-coding shows percentage of identity. The REM1.3 S74, T81 and S91 sites are highlighted.

(B) *Left*, Representative epifluorescence microscopy images of PVX-GFP infection foci on *N. benthamiana* leaf epidermal cells transiently expressing RFP-REM1.3, RFP-*AtREM1.2* or RFP-*AtREM1.3* at 5 DAI. Scale bar indicate 400 μ m. *Right*, Graph represents the relative PVX-GFP infection foci area in the presence of RFP-REM1.3 or Arabidopsis homologs compared to mock control (co-infiltration of PVX-GFP with empty *A. tumefaciens* strain). At least 184 foci per condition in 4 independent biological repeats were measured. Statistical differences are indicated by letters as revealed by Dunn's multiple comparisons test $p < 0.001$. (TIF)

S6 Fig. *In vitro* characterization of REM1.3 phosphorylation conditions. Autoradiography reveals *in vitro* phosphorylated 6His-REM1.3N (A) or 6His-REM1.3 (B) by microsomal extracts of healthy *N. benthamiana* leaves in the presence of increasing concentrations of staurosporine (A) or Polylysine, β -glycerophosphate (BGP), GTP, AMP and ATP (B). (C) Effect of Ca^{2+} and EGTA on 6His-REM1.3^N phosphorylation by kinase(s) in microsomal extracts. (TIF)

S7 Fig. AtCPK3CAD202A dead mutant does not phosphorylate REM1.3 *in vitro*. AtCPK3-CA-HA and AtCPK3CAD202A-HA were expressed in *Arabidopsis thaliana* mesophyll protoplasts. Immunoprecipitated proteins were incubated with ATP [γ -³³P] and submitted to an *in vitro* kinase assay using 6His-REM1.3 or histone as substrates. *In vitro* kinase assays were revealed by autoradiography. Trans-phosphorylation of the substrates 6His-REM1.3 or histone is indicated. Western blot against HA shows the expression levels of the expressed proteins. (TIF)

S8 Fig. Stable transgenic lines *N. benthamiana* under-expressing group 1 REMORINs. (A) Protein expression levels of endogenous NbREMs in the hpREM lines, determined by Western Blot analysis using anti-REM1.3 antibodies. Protein extracts from three independent plants per line were used, namely lines 1.4, 2.1, 10.2. (B) Expression of endogenous NbREMs in the hpREM lines determined by RT-qPCR analysis. Results are expressed relative to the NbREMs expression levels in the WT background. RT-qPCR signals were normalized to actin levels. (C) PVX-GFP spreading is accelerated in the hpREM lines. Graph represents the PVX-GFP infection foci area in the different hpREM lines compared to WT. At least three independent experiments were performed. Error bars show +/- SEM. Statistical differences compared to WT were determined by Mann-Whitney test *** $p < 0.001$. (D) PVX systemic propagation is inversely correlated with REM levels in 4-week-old transgenic *N. benthamiana* leaves. Viral charges were assayed by DAS ELISA using antibodies to PVX coat protein (diluted on 1/100) on distal leaves (at 3 nodes above the inoculated leaves) at 10 DAI. 3 independent experiments were performed with eight plants for each hpREM transgenic line and WT or empty vector control (mock). Error bars show SE, and significance is assessed by Mann-Whitney non-parametric test (*, $P < 0.1$; **, $P < 0.05$; ***, $P < 0.001$). (TIF)

Acknowledgments

Imaging was performed at the Bordeaux Imaging Center, member of the national infrastructure France BioImaging. We acknowledge Dr S. P. Dinesh-Kumar for the gift of TMV-GFP clone, Dr Alicia Zelada for the gift of PVX Δ TGBp1 and viral protein constructs and Ms Coralie Chesseron for greenhouse facilities.

Author Contributions

Conceptualization: Artemis Perraki, Julien Gronnier, Paul Gouguet, Marie Boudsocq, Cyril Zipfel, Emmanuelle Bayer, Sébastien Mongrand, Véronique Germain.

Data curation: Artemis Perraki, Paul Gouguet, Marie Boudsocq, Sébastien Mongrand.

Formal analysis: Artemis Perraki, Julien Gronnier, Paul Gouguet, Marie Boudsocq, Anne-Flore Deroubaix, Sébastien Mongrand.

Funding acquisition: Artemis Perraki, Cyril Zipfel, Sébastien Mongrand.

Investigation: Artemis Perraki, Julien Gronnier, Paul Gouguet, Marie Boudsocq, Anne-Flore Deroubaix, Vincent Simon, Sylvie German-Retana, Anthony Legrand, Sébastien Mongrand, Véronique Germain.

Methodology: Artemis Perraki, Julien Gronnier, Paul Gouguet, Marie Boudsocq, Vincent Simon, Sylvie German-Retana, Birgit Habenstein, Emmanuelle Bayer, Sébastien Mongrand, Véronique Germain.

Project administration: Sébastien Mongrand.

Resources: Artemis Perraki, Julien Gronnier, Marie Boudsocq, Vincent Simon, Sylvie German-Retana, Birgit Habenstein, Cyril Zipfel, Emmanuelle Bayer, Sébastien Mongrand, Véronique Germain.

Software: Julien Gronnier.

Supervision: Birgit Habenstein, Sébastien Mongrand, Véronique Germain.

Validation: Artemis Perraki, Julien Gronnier, Sébastien Mongrand.

Visualization: Artemis Perraki, Julien Gronnier, Paul Gouguet, Anne-Flore Deroubaix, Anthony Legrand, Sébastien Mongrand.

Writing – original draft: Artemis Perraki, Julien Gronnier, Paul Gouguet, Sébastien Mongrand, Véronique Germain.

Writing – review & editing: Artemis Perraki, Julien Gronnier, Paul Gouguet, Marie Boudsocq, Emmanuelle Bayer, Sébastien Mongrand, Véronique Germain.

References

1. Nicolson GL. The Fluid-Mosaic Model of Membrane Structure: still relevant to understanding the structure, function and dynamics of biological membranes after more than 40 years. *Biochimica et biophysica acta*. 2014; 1838(6):1451–66. <https://doi.org/10.1016/j.bbamem.2013.10.019> PMID: 24189436.
2. Sezgin E, Levental I, Mayor S, Eggeling C. The mystery of membrane organization: composition, regulation and roles of lipid rafts. *Nature reviews Molecular cell biology*. 2017; 18(6):361–74. <https://doi.org/10.1038/nrm.2017.16> PMID: 28356571; PubMed Central PMCID: PMC500228.
3. Lingwood D, Simons K. Lipid rafts as a membrane-organizing principle. *Science*. 2010; 327(5961):46–50. <https://doi.org/10.1126/science.1174621> PMID: 20044567.
4. Simons K, Gerl MJ. Revitalizing membrane rafts: new tools and insights. *Nature reviews Molecular cell biology*. 2010; 11(10):688–99. Epub 2010/09/24. doi: nrm2977 [pii] <https://doi.org/10.1038/nrm2977> PMID: 20861879.
5. Kusumi A, Fujiwara TK, Chadda R, Xie M, Tsunoyama TA, Kalay Z, et al. Dynamic organizing principles of the plasma membrane that regulate signal transduction: commemorating the fortieth anniversary of Singer and Nicolson's fluid-mosaic model. *Annu Rev Cell Dev Biol*. 2012; 28:215–50. <https://doi.org/10.1146/annurev-cellbio-100809-151736> PMID: 22905956.
6. Mugler A, Tostevin F, ten Wolde PR. Spatial partitioning improves the reliability of biochemical signaling. *Proceedings of the National Academy of Sciences of the United States of America*. 2013; 110(15):5927–32. <https://doi.org/10.1073/pnas.1218301110> PMID: 23530194; PubMed Central PMCID: PMC3625283.
7. Bucherl CA, Jarsch IK, Schudoma C, Segonzac C, Mbengue M, Robatzek S, et al. Plant immune and growth receptors share common signalling components but localise to distinct plasma membrane nanodomains. *Elife*. 2017; 6. <https://doi.org/10.7554/eLife.25114> PMID: 28262094; PubMed Central PMCID: PMC5383397.
8. Raffaele S, Bayer E, Lafarge D, Cluzet S, German Retana S, Boubekur T, et al. Remorin, a solanaceae protein resident in membrane rafts and plasmodesmata, impairs potato virus X movement. *The Plant cell*. 2009; 21(5):1541–55. Epub 2009/05/28. doi: tpc.108.064279 [pii] <https://doi.org/10.1105/tpc.108.064279> PMID: 19470590; PubMed Central PMCID: PMC2700541.

9. Jarsch IK, Ott T. Perspectives on remorin proteins, membrane rafts, and their role during plant-microbe interactions. *Molecular plant-microbe interactions: MPMI*. 2011; 24(1):7–12. <https://doi.org/10.1094/MPMI-07-10-0166> PMID: 21138374.
10. Jarsch IK, Konrad SS, Stratil TF, Urbanus SL, Szymanski W, Braun P, et al. Plasma Membranes Are Subcompartmentalized into a Plethora of Coexisting and Diverse Microdomains in Arabidopsis and *Nicotiana benthamiana*. *The Plant cell*. 2014; 26(4):1698–711. <https://doi.org/10.1105/tpc.114.124446> PMID: 24714763; PubMed Central PMCID: PMC4036580.
11. Lefebvre B, Timmers T, Mbengue M, Moreau S, Herve C, Toth K, et al. A remorin protein interacts with symbiotic receptors and regulates bacterial infection. *Proceedings of the National Academy of Sciences of the United States of America*. 2010; 107(5):2343–8. <https://doi.org/10.1073/pnas.0913320107> PMID: 20133878; PubMed Central PMCID: PMC2836688.
12. Gui J, Zheng S, Liu C, Shen J, Li J, Li L. OsREM4.1 Interacts with OsSERK1 to Coordinate the Interlinking between Abscisic Acid and Brassinosteroid Signaling in Rice. *Dev Cell*. 2016; 38(2):201–13. <https://doi.org/10.1016/j.devcel.2016.06.011> PMID: 27424498.
13. Raffaele S, Perraki A, Mongrand S. The Remorin C-terminal Anchor was shaped by convergent evolution among membrane binding domains. *Plant signaling & behavior*. 2013; 8(3). Epub 2013/01/10. <https://doi.org/10.4161/psb.23207> PMID: 23299327; PubMed Central PMCID: PMC3676492.
14. Perraki A, Cacas JL, Crowet JM, Lins L, Castroviejo M, German-Retana S, et al. Plasma membrane localization of *Solanum tuberosum* remorin from group 1, homolog 3 is mediated by conformational changes in a novel C-terminal anchor and required for the restriction of potato virus X movement]. *Plant physiology*. 2012; 160(2):624–37. Epub 2012/08/03. <https://doi.org/10.1104/pp.112.200519> PMID: 22855937; PubMed Central PMCID: PMC3461544.
15. Martinez D, Legrand A, Gronnier J, Decossas M, Gouguet P, Lambert O, et al. Coiled-coil oligomerization controls localization of the plasma membrane REMORINs. *J Struct Biol*. 2018. <https://doi.org/10.1016/j.jsb.2018.02.003> PMID: 29481850.
16. Toth K, Stratil TF, Madsen EB, Ye J, Popp C, Antolin-Llovera M, et al. Functional domain analysis of the Remorin protein LjSYMREM1 in *Lotus japonicus*. *PloS one*. 2012; 7(1):e30817. <https://doi.org/10.1371/journal.pone.0030817> PMID: 22292047; PubMed Central PMCID: PMC3264624.
17. Son S, Oh CJ, An CS. Arabidopsis thaliana Remorins Interact with SnRK1 and Play a Role in Susceptibility to Beet Curly Top Virus and Beet Severe Curly Top Virus. *The plant pathology journal*. 2014; 30(3):269–78. <https://doi.org/10.5423/PPJ.OA.06.2014.0061> PMID: 25289013; PubMed Central PMCID: PMC4181108.
18. Jamann TM, Luo X, Morales L, Kolkman JM, Chung CL, Nelson RJ. A remorin gene is implicated in quantitative disease resistance in maize. *Theor Appl Genet*. 2016; 129(3):591–602. <https://doi.org/10.1007/s00122-015-2650-6> PMID: 26849237.
19. Checker VG, Khurana P. Molecular and functional characterization of mulberry EST encoding remorin (MiREM) involved in abiotic stress. *Plant Cell Rep*. 2013; 32(11):1729–41. <https://doi.org/10.1007/s00299-013-1483-5> PMID: 23942844.
20. Yue J, Li C, Liu Y, Yu J. A remorin gene SiREM6, the target gene of SiARDP, from foxtail millet (*Setaria italica*) promotes high salt tolerance in transgenic Arabidopsis. *PloS one*. 2014; 9(6):e100772. <https://doi.org/10.1371/journal.pone.0100772> PMID: 24967625; PubMed Central PMCID: PMC4072699.
21. Gronnier J, Gerbeau-Pissot P, Germain V, Mongrand S, Simon-Plas F. Divide and Rule: Plant Plasma Membrane Organization. *Trends in plant science*. 2018. <https://doi.org/10.1016/j.tplants.2018.07.007> PMID: 30174194.
22. Fernandez-Calvino L, Faulkner C, Walshaw J, Saalbach G, Bayer E, Benitez-Alfonso Y, et al. Arabidopsis plasmodesmal proteome. *PloS one*. 2011; 6(4):e18880. Epub 2011/05/03. <https://doi.org/10.1371/journal.pone.0018880> PMID: 21533090; PubMed Central PMCID: PMC3080382.
23. Gui J, Zheng S, Shen J, Li L. Grain setting defect1 (GSD1) function in rice depends on S-acylation and interacts with actin 1 (OsACT1) at its C-terminal. *Frontiers in plant science*. 2015; 6:804. <https://doi.org/10.3389/fpls.2015.00804> PMID: 26483819; PubMed Central PMCID: PMC4590517.
24. Tilsner J, Nicolas W, Rosado A, Bayer EM. Staying Tight: Plasmodesmal Membrane Contact Sites and the Control of Cell-to-Cell Connectivity in Plants. *Annu Rev Plant Biol*. 2016; 67:337–64. <https://doi.org/10.1146/annurev-arplant-043015-111840> PMID: 26905652.
25. Nicolas WJ, Grison MS, Trepout S, Gaston A, Fouche M, Cordelieres FP, et al. Architecture and permeability of post-cytokinesis plasmodesmata lacking cytoplasmic sleeves. *Nat Plants*. 2017; 3:17082. <https://doi.org/10.1038/nplants.2017.82> PMID: 28604682.
26. Grison MS, Brocard L, Fouillen L, Nicolas W, Wewer V, Dormann P, et al. Specific membrane lipid composition is important for plasmodesmata function in Arabidopsis. *The Plant cell*. 2015; 27

- (4):1228–50. <https://doi.org/10.1105/tpc.114.135731> PMID: 25818623; PubMed Central PMCID: PMCPMC4558693.
27. Lee JY, Wang X, Cui W, Sager R, Modla S, Czymbek K, et al. A plasmodesmata-localized protein mediates crosstalk between cell-to-cell communication and innate immunity in Arabidopsis. *The Plant cell*. 2011; 23(9):3353–73. <https://doi.org/10.1105/tpc.111.087742> PMID: 21934146; PubMed Central PMCID: PMCPMC3203451.
 28. Zavaliev R, Dong X, Epel BL. Glycosylphosphatidylinositol (GPI) Modification Serves as a Primary Plasmodesmal Sorting Signal. *Plant physiology*. 2016; 172(2):1061–73. <https://doi.org/10.1104/pp.16.01026> PMID: 27559035; PubMed Central PMCID: PMCPMC5047108.
 29. Chen XY, Kim JY. Callose synthesis in higher plants. *Plant signaling & behavior*. 2009; 4(6):489–92. <https://doi.org/10.4161/psb.4.6.8359> PMID: 19816126; PubMed Central PMCID: PMCPMC2688293.
 30. Angell SM, Davies C, Baulcombe DC. Cell-to-cell movement of potato virus X is associated with a change in the size-exclusion limit of plasmodesmata in trichome cells of *Nicotiana glauca*. *Virology*. 1996; 216(1):197–201. Epub 1996/02/01. doi: S0042-6822(96)90046-X [pii] <https://doi.org/10.1006/viro.1996.0046> PMID: 8614986.
 31. Howard AR, Heppler ML, Ju HJ, Krishnamurthy K, Payton ME, Verchot-Lubicz J. Potato virus X TGBp1 induces plasmodesmata gating and moves between cells in several host species whereas CP moves only in *N. benthamiana* leaves. *Virology*. 2004; 328(2):185–97. Epub 2004/10/07. doi: S0042-6822(04)00399-X [pii] <https://doi.org/10.1016/j.virol.2004.06.039> PMID: 15464839.
 32. Raffaele S, Mongrand S, Gamas P, Niebel A, Ott T. Genome-wide annotation of remorins, a plant-specific protein family: evolutionary and functional perspectives. *Plant physiology*. 2007; 145(3):593–600. Epub 2007/11/07. <https://doi.org/10.1104/pp.107.108639> PMID: 17984200; PubMed Central PMCID: PMC2048807.
 33. Perraki A, Binaghi M, Mecchia MA, Gronnier J, German-Retana S, Mongrand S, et al. StRemorin1.3 hampers Potato virus X TGBp1 ability to increase plasmodesmata permeability, but does not interfere with its silencing suppressor activity. *FEBS letters*. 2014; 588(9):1699–705. <https://doi.org/10.1016/j.febslet.2014.03.014> PMID: 24657438.
 34. Jaubert M, Bhattacharjee S, Mello AF, Perry KL, Moffett P. ARGONAUTE2 mediates RNA-silencing antiviral defenses against Potato virus X in Arabidopsis. *Plant physiology*. 2011; 156(3):1556–64. <https://doi.org/10.1104/pp.111.178012> PMID: 21576511; PubMed Central PMCID: PMCPMC3135937.
 35. Goodin MM, Zaitlin D, Naidu RA, Lommel SA. *Nicotiana benthamiana*: Its History and Future as a Model for Plant-Pathogen Interactions. *Molecular plant-microbe interactions: MPMI*. 2015; 2015(1):28–39. <https://doi.org/10.1094/MPMI-00-00-1015-REV.testissue> PMID: 27839076.
 36. Gronnier J, Crowet JM, Habenstein B, Nasir MN, Bayle V, Hosy E, et al. Structural basis for plant plasma membrane protein dynamics and organization into functional nanodomains. *Elife*. 2017; 6. <https://doi.org/10.7554/eLife.26404> PMID: 28758890; PubMed Central PMCID: PMCPMC5536944.
 37. Farmer EE, Moloshok TD, Saxton MJ, Ryan CA. Oligosaccharide signaling in plants. Specificity of oliguronide-enhanced plasma membrane protein phosphorylation. *The Journal of biological chemistry*. 1991; 266(5):3140–5. PMID: 1993685.
 38. Reymond P, Kunz B, Paul-Pletzer K, Grimm R, Eckerskorn C, Farmer EE. Cloning of a cDNA encoding a plasma membrane-associated, uronide binding phosphoprotein with physical properties similar to viral movement proteins. *The Plant cell*. 1996; 8(12):2265–76. <https://doi.org/10.1105/tpc.8.12.2265> PMID: 8989883; PubMed Central PMCID: PMC161351.
 39. Benschop JJ, Mohammed S, O'Flaherty M, Heck AJ, Slijper M, Menke FL. Quantitative phosphoproteomics of early elicitor signaling in Arabidopsis. *Molecular & cellular proteomics: MCP*. 2007; 6(7):1198–214. <https://doi.org/10.1074/mcp.M600429-MCP200> PMID: 17317660.
 40. Widjaja I, Naumann K, Roth U, Wolf N, Mackey D, Dangl JL, et al. Combining subproteome enrichment and Rubisco depletion enables identification of low abundance proteins differentially regulated during plant defense. *Proteomics*. 2009; 9(1):138–47. <https://doi.org/10.1002/pmic.200800293> PMID: 19053141.
 41. Tilsner J, Linnik O, Louveaux M, Roberts IM, Chapman SN, Oparka KJ. Replication and trafficking of a plant virus are coupled at the entrances of plasmodesmata. *J Cell Biol*. 2013; 201(7):981–95. <https://doi.org/10.1083/jcb.201304003> PMID: 23798728; PubMed Central PMCID: PMCPMC3691464.
 42. Bozkurt TO, Richardson A, Dagdas YF, Mongrand S, Kamoun S, Raffaele S. The Plant Membrane-Associated REMORIN1.3 Accumulates in Discrete Perihäustorial Domains and Enhances Susceptibility to *Phytophthora infestans*. *Plant physiology*. 2014; 165(3):1005–18. <https://doi.org/10.1104/pp.114.235804> PMID: 24808104; PubMed Central PMCID: PMC4081318.

43. Scholthof KB, Adkins S, Czosnek H, Palukaitis P, Jacquot E, Hohn T, et al. Top 10 plant viruses in molecular plant pathology. *Molecular plant pathology*. 2011; 12(9):938–54. <https://doi.org/10.1111/j.1364-3703.2011.00752.x> PMID: 22017770.
44. Kusumi A, Suzuki K. Toward understanding the dynamics of membrane-raft-based molecular interactions. *Biochimica et biophysica acta*. 2005; 1746(3):234–51. Epub 2005/12/22. <https://doi.org/10.1016/j.bbamcr.2005.10.001> PMID: 16368465.
45. Hosy E, Martiniere A, Choquet D, Maurel C, Luu DT. Super-resolved and dynamic imaging of membrane proteins in plant cells reveal contrasting kinetic profiles and multiple confinement mechanisms. *Molecular plant*. 2015; 8(2):339–42. <https://doi.org/10.1016/j.molp.2014.10.006> PMID: 25680779.
46. Manley S, Gillette JM, Patterson GH, Shroff H, Hess HF, Betzig E, et al. High-density mapping of single-molecule trajectories with photoactivated localization microscopy. *Nat Methods*. 2008; 5(2):155–7. <https://doi.org/10.1038/nmeth.1176> PMID: 18193054.
47. Wiedenmann J, Ivanchenko S, Oswald F, Schmitt F, Rocker C, Salih A, et al. EosFP, a fluorescent marker protein with UV-inducible green-to-red fluorescence conversion. *Proceedings of the National Academy of Sciences of the United States of America*. 2004; 101(45):15905–10. <https://doi.org/10.1073/pnas.0403668101> PMID: 15505211; PubMed Central PMCID: PMC528746.
48. Martiniere A, Lavagi I, Nageswaran G, Rolfe DJ, Maneta-Peyret L, Luu DT, et al. Cell wall constrains lateral diffusion of plant plasma-membrane proteins. *Proceedings of the National Academy of Sciences of the United States of America*. 2012; 109(31):12805–10. Epub 2012/06/13. <https://doi.org/10.1073/pnas.1202040109> PMID: 22689944; PubMed Central PMCID: PMC3411962.
49. Konrad SS, Popp C, Stratil TF, Jarsch IK, Thallmair V, Folgmann J, et al. S-acylation anchors remorin proteins to the plasma membrane but does not primarily determine their localization in membrane microdomains. *The New phytologist*. 2014; 203(3):758–69. <https://doi.org/10.1111/nph.12867> PMID: 24897938.
50. Levet F, Hosy E, Kechkar A, Butler C, Beghin A, Choquet D, et al. SR-Tesseler: a method to segment and quantify localization-based super-resolution microscopy data. *Nat Methods*. 2015; 12(11):1065–71. <https://doi.org/10.1038/nmeth.3579> PMID: 26344046.
51. Calil IP, Fontes EPB. Plant immunity against viruses: antiviral immune receptors in focus. *Ann Bot*. 2017; 119(5):711–23. <https://doi.org/10.1093/aob/mcw200> PMID: 27780814.
52. Nicaise V, Candresse T. Plum pox virus capsid protein suppresses plant pathogen-associated molecular pattern (PAMP)-triggered immunity. *Molecular plant pathology*. 2017; 18(6):878–86. <https://doi.org/10.1111/mpp.12447> PMID: 27301551.
53. de Ronde D, Butterbach P, Kormelink R. Dominant resistance against plant viruses. *Frontiers in plant science*. 2014; 5:307. <https://doi.org/10.3389/fpls.2014.00307> PMID: 25018765; PubMed Central PMCID: PMC4073217.
54. de Ronde D, Pasquier A, Ying S, Butterbach P, Lohuis D, Kormelink R. Analysis of Tomato spotted wilt virus NSs protein indicates the importance of the N-terminal domain for avirulence and RNA silencing suppression. *Molecular plant pathology*. 2014; 15(2):185–95. <https://doi.org/10.1111/mpp.12082> PMID: 24103150.
55. Gouveia BC, Calil IP, Machado JP, Santos AA, Fontes EP. Immune Receptors and Co-receptors in Antiviral Innate Immunity in Plants. *Front Microbiol*. 2016; 7:2139. <https://doi.org/10.3389/fmicb.2016.02139> PMID: 28105028; PubMed Central PMCID: PMC45214455.
56. Niehl A, Appaix F, Bosca S, van der Sanden B, Nicoud JF, Bolze F, et al. Fluorescent Tobacco mosaic virus-Derived Bio-Nanoparticles for Intravital Two-Photon Imaging. *Frontiers in plant science*. 2015; 6:1244. <https://doi.org/10.3389/fpls.2015.01244> PMID: 26793221; PubMed Central PMCID: PMC4710741.
57. Marin M, Ott T. Phosphorylation of intrinsically disordered regions in remorin proteins. *Frontiers in plant science*. 2012; 3:86. <https://doi.org/10.3389/fpls.2012.00086> PMID: 22639670; PubMed Central PMCID: PMC3355724.
58. Cluzet S. Etude du rôle de la rémorine dans la défense végétale. Thèse de doctorat, Université de Lausanne. 2001.
59. Mongrand S, Morel J, Laroche J, Claverol S, Carde JP, Hartmann MA, et al. Lipid rafts in higher plant cells: purification and characterization of Triton X-100-insoluble microdomains from tobacco plasma membrane. *The Journal of biological chemistry*. 2004; 279(35):36277–86. Epub 2004/06/11. <https://doi.org/10.1074/jbc.M403440200> PMID: 15190066.
60. Kalay Z. Reaction kinetics in the plasma membrane. *Biotechnol J*. 2012; 7(6):745–52. <https://doi.org/10.1002/biot.201100362> PMID: 22378739.
61. Tian T, Harding A, Inder K, Plowman S, Parton RG, Hancock JF. Plasma membrane nanoswitches generate high-fidelity Ras signal transduction. *Nature cell biology*. 2007; 9(8):905–14. <https://doi.org/10.1038/ncb1615> PMID: 17618274.

62. Furt F, Konig S, Bessoule JJ, Sargueil F, Zallot R, Stanislas T, et al. Polyphosphoinositides are enriched in plant membrane rafts and form microdomains in the plasma membrane. *Plant physiology*. 2010; 152(4):2173–87. Epub 2010/02/26. doi: pp.109.149823 [pii] <https://doi.org/10.1104/pp.109.149823> PMID: 20181756; PubMed Central PMCID: PMC2850013.
63. Meggio F, Donella Deana A, Ruzzene M, Brunati AM, Cesaro L, Guerra B, et al. Different susceptibility of protein kinases to staurosporine inhibition. Kinetic studies and molecular bases for the resistance of protein kinase CK2. *European journal of biochemistry / FEBS*. 1995; 234(1):317–22. PMID: 8529658.
64. Ruegg UT, Burgess GM. Staurosporine, K-252 and UCN-01: potent but nonspecific inhibitors of protein kinases. *Trends Pharmacol Sci*. 1989; 10(6):218–20. PMID: 2672462.
65. Meggio F, Pinna LA. One-thousand-and-one substrates of protein kinase CK2? *FASEB journal: official publication of the Federation of American Societies for Experimental Biology*. 2003; 17(3):349–68. <https://doi.org/10.1096/fj.02-0473rev> PMID: 12631575.
66. Binder BM, Harper JF, Sussman MR. Characterization of an Arabidopsis calmodulin-like domain protein kinase purified from *Escherichia coli* using an affinity sandwich technique. *Biochemistry*. 1994; 33(8):2033–41. PMID: 8117660.
67. Boudsocq M, Sheen J. CDPKs in immune and stress signaling. *Trends in plant science*. 2013; 18(1):30–40. <https://doi.org/10.1016/j.tplants.2012.08.008> PMID: 22974587; PubMed Central PMCID: PMC3534830.
68. Schulz P, Herde M, Romeis T. Calcium-dependent protein kinases: hubs in plant stress signaling and development. *Plant physiology*. 2013; 163(2):523–30. <https://doi.org/10.1104/pp.113.222539> PMID: 24014579; PubMed Central PMCID: PMC3793034.
69. Boudsocq M, Droillard MJ, Regad L, Lauriere C. Characterization of Arabidopsis calcium-dependent protein kinases: activated or not by calcium? *The Biochemical journal*. 2012; 447(2):291–9. <https://doi.org/10.1042/BJ20112072> PMID: 22827269.
70. Kierszniowska S, Seiwert B, Schulze WX. Definition of Arabidopsis sterol-rich membrane microdomains by differential treatment with methyl-beta-cyclodextrin and quantitative proteomics. *Molecular & cellular proteomics: MCP*. 2009; 8(4):612–23. Epub 2008/11/28. doi: M800346-MCP200 [pii] <https://doi.org/10.1074/mcp.M800346-MCP200> PMID: 19036721; PubMed Central PMCID: PMC2667346.
71. Mehlmer N, Wurzinger B, Stael S, Hofmann-Rodrigues D, Csaszar E, Pfister B, et al. The Ca(2+)-dependent protein kinase CPK3 is required for MAPK-independent salt-stress acclimation in Arabidopsis. *The Plant journal: for cell and molecular biology*. 2010; 63(3):484–98. <https://doi.org/10.1111/j.1365-313X.2010.04257.x> PMID: 20497378; PubMed Central PMCID: PMC32988408.
72. Demir F, Hortrich C, Blachutzik JO, Scherzer S, Reinders Y, Kierszniowska S, et al. Arabidopsis nanodomain-delimited ABA signaling pathway regulates the anion channel SLAH3. *Proceedings of the National Academy of Sciences of the United States of America*. 2013; 110(20):8296–301. <https://doi.org/10.1073/pnas.1211667110> PMID: 23630285; PubMed Central PMCID: PMC3657796.
73. Harmon AC, Gribskov M, Harper JF. CDPKs—a kinase for every Ca²⁺ signal? *Trends in plant science*. 2000; 5(4):154–9. PMID: 10740296.
74. Harper JF, Breton G, Harmon A. Decoding Ca(2+) signals through plant protein kinases. *Annu Rev Plant Biol*. 2004; 55:263–88. <https://doi.org/10.1146/annurev.arplant.55.031903.141627> PMID: 15377221.
75. Ubersax JA, Ferrell JE Jr., Mechanisms of specificity in protein phosphorylation. *Nature reviews Molecular cell biology*. 2007; 8(7):530–41. <https://doi.org/10.1038/nrm2203> PMID: 17585314.
76. Bah A, Vernon RM, Siddiqui Z, Krzeminski M, Muhandiram R, Zhao C, et al. Folding of an intrinsically disordered protein by phosphorylation as a regulatory switch. *Nature*. 2015; 519(7541):106–9. <https://doi.org/10.1038/nature13999> PMID: 25533957.
77. Gui J, Liu C, Shen J, Li L. Grain setting defect1, encoding a remorin protein, affects the grain setting in rice through regulating plasmodesmatal conductance. *Plant physiology*. 2014; 166(3):1463–78. <https://doi.org/10.1104/pp.114.246769> PMID: 25253885; PubMed Central PMCID: PMC4226345.
78. Incarbone M, Dunoyer P. RNA silencing and its suppression: novel insights from in planta analyses. *Trends in plant science*. 2013; 18(7):382–92. <https://doi.org/10.1016/j.tplants.2013.04.001> PMID: 23684690.
79. Carr JP, Loebenstein G. Natural and engineered resistance to plant viruses, part II. Preface. *Adv Virus Res*. 2010; 76:vii. [https://doi.org/10.1016/S0065-3527\(10\)76011-5](https://doi.org/10.1016/S0065-3527(10)76011-5) PMID: 20362221.
80. Zorzatto C, Machado JP, Lopes KV, Nascimento KJ, Pereira WA, Brustolini OJ, et al. NIK1-mediated translation suppression functions as a plant antiviral immunity mechanism. *Nature*. 2015; 520(7549):679–82. <https://doi.org/10.1038/nature14171> PMID: 25707794; PubMed Central PMCID: PMC4779052.

81. Zipfel C. Plant pattern-recognition receptors. *Trends Immunol.* 2014; 35(7):345–51. <https://doi.org/10.1016/j.it.2014.05.004> PMID: 24946686.
82. Dodds PN, Rathjen JP. Plant immunity: towards an integrated view of plant-pathogen interactions. *Nat Rev Genet.* 2010; 11(8):539–48. <https://doi.org/10.1038/nrg2812> PMID: 20585331.
83. Dangl JL, Horvath DM, Staskawicz BJ. Pivoting the plant immune system from dissection to deployment. *Science.* 2013; 341(6147):746–51. <https://doi.org/10.1126/science.1236011> PMID: 23950531; PubMed Central PMCID: PMC3869199.
84. Kroner A, Hamelin G, Andrivon D, Val F. Quantitative resistance of potato to *Pectobacterium atrosepticum* and *Phytophthora infestans*: integrating PAMP-triggered response and pathogen growth. *PLoS one.* 2011; 6(8):e23331. <https://doi.org/10.1371/journal.pone.0023331> PMID: 21853112; PubMed Central PMCID: PMC3154927.
85. Hanssen IM, van Esse HP, Ballester AR, Hogewoning SW, Parra NO, Paeleman A, et al. Differential tomato transcriptomic responses induced by pepino mosaic virus isolates with differential aggressiveness. *Plant physiology.* 2011; 156(1):301–18. <https://doi.org/10.1104/pp.111.173906> PMID: 21427280; PubMed Central PMCID: PMC3091055.
86. Love AJ, Yun BW, Laval V, Loake GJ, Milner JJ. Cauliflower mosaic virus, a compatible pathogen of *Arabidopsis*, engages three distinct defense-signaling pathways and activates rapid systemic generation of reactive oxygen species. *Plant physiology.* 2005; 139(2):935–48. <https://doi.org/10.1104/pp.105.066803> PMID: 16169957; PubMed Central PMCID: PMC31256007.
87. Whitham SA, Quan S, Chang HS, Cooper B, Estes B, Zhu T, et al. Diverse RNA viruses elicit the expression of common sets of genes in susceptible *Arabidopsis thaliana* plants. *The Plant journal: for cell and molecular biology.* 2003; 33(2):271–83. PMID: 12535341.
88. Jones JD, Dangl JL. The plant immune system. *Nature.* 2006; 444(7117):323–9. <https://doi.org/10.1038/nature05286> PMID: 17108957.
89. Mandadi KK, Scholthof KB. Plant immune responses against viruses: how does a virus cause disease? *The Plant cell.* 2013; 25(5):1489–505. <https://doi.org/10.1105/tpc.113.111658> PMID: 23709626; PubMed Central PMCID: PMC3694688.
90. Levy A, Zheng JY, Lazarowitz SG. Synaptotagmin SYTA forms ER-plasma membrane junctions that are recruited to plasmodesmata for plant virus movement. *Current biology: CB.* 2015; 25(15):2018–25. <https://doi.org/10.1016/j.cub.2015.06.015> PMID: 26166780; PubMed Central PMCID: PMC4526382.
91. Fu S, Xu Y, Li C, Li Y, Wu J, Zhou X. Rice Stripe Virus Interferes with S-acylation of Remorin and Induces Its Autophagic Degradation to Facilitate Virus Infection. *Molecular plant.* 2018; 11(2):269–87. <https://doi.org/10.1016/j.molp.2017.11.011> PMID: 29229567.
92. Mori IC, Murata Y, Yang Y, Munemasa S, Wang YF, Andreoli S, et al. CDPKs CPK6 and CPK3 function in ABA regulation of guard cell S-type anion- and Ca(2+)-permeable channels and stomatal closure. *PLoS Biol.* 2006; 4(10):e327. <https://doi.org/10.1371/journal.pbio.0040327> PMID: 17032064; PubMed Central PMCID: PMC1592316.
93. Latz A, Mehler N, Zapf S, Mueller TD, Wurzing B, Pfister B, et al. Salt stress triggers phosphorylation of the *Arabidopsis* vacuolar K⁺ channel TPK1 by calcium-dependent protein kinases (CDPKs). *Molecular plant.* 2013; 6(4):1274–89. <https://doi.org/10.1093/mp/sss158> PMID: 23253603; PubMed Central PMCID: PMC3971370.
94. Kanchiswamy CN, Takahashi H, Quadro S, Maffei ME, Bossi S, Berteau C, et al. Regulation of *Arabidopsis* defense responses against *Spodoptera littoralis* by CPK-mediated calcium signaling. *BMC plant biology.* 2010; 10:97. <https://doi.org/10.1186/1471-2229-10-97> PMID: 20504319; PubMed Central PMCID: PMC3095362.
95. Shabala S, Babourina O, Rengel Z, Nemchinov LG. Non-invasive microelectrode potassium flux measurements as a potential tool for early recognition of virus-host compatibility in plants. *Planta.* 2010; 232(4):807–15. <https://doi.org/10.1007/s00425-010-1213-y> PMID: 20623138.
96. Takabatake R, Karita E, Seo S, Mitsuhashi I, Kuchitsu K, Ohashi Y. Pathogen-induced calmodulin isoforms in basal resistance against bacterial and fungal pathogens in tobacco. *Plant Cell Physiol.* 2007; 48(3):414–23. <https://doi.org/10.1093/pcp/pcm011> PMID: 17251204.
97. Nakahara KS, Masuta C, Yamada S, Shimura H, Kashihara Y, Wada TS, et al. Tobacco calmodulin-like protein provides secondary defense by binding to and directing degradation of virus RNA silencing suppressors. *Proceedings of the National Academy of Sciences of the United States of America.* 2012; 109(25):10113–8. <https://doi.org/10.1073/pnas.1201628109> PMID: 22665793; PubMed Central PMCID: PMC3382489.
98. Iakoucheva LM, Radivojac P, Brown CJ, O'Connor TR, Sikes JG, Obradovic Z, et al. The importance of intrinsic disorder for protein phosphorylation. *Nucleic acids research.* 2004; 32(3):1037–49. <https://doi.org/10.1093/nar/gkh253> PMID: 14960716; PubMed Central PMCID: PMC373391.

99. Cotellet V, Leonhardt N. 14-3-3 Proteins in Guard Cell Signaling. *Frontiers in plant science*. 2015; 6:1210. <https://doi.org/10.3389/fpls.2015.01210> PMID: 26858725; PubMed Central PMCID: PMC4729941.
100. Karimi M, Inze D, Depicker A. GATEWAY vectors for Agrobacterium-mediated plant transformation. *Trends in plant science*. 2002; 7(5):193–5. PMID: 11992820.
101. Taton M, Husselstein T, Benveniste P, Rahier A. Role of highly conserved residues in the reaction catalyzed by recombinant Delta7-sterol-C5(6)-desaturase studied by site-directed mutagenesis. *Biochemistry*. 2000; 39(4):701–11. PMID: 10651635.
102. Martin K, Kopperud K, Chakrabarty R, Banerjee R, Brooks R, Goodin MM. Transient expression in *Nicotiana benthamiana* fluorescent marker lines provides enhanced definition of protein localization, movement and interactions in planta. *The Plant journal: for cell and molecular biology*. 2009; 59(1):150–62. <https://doi.org/10.1111/j.1365-313X.2009.03850.x> PMID: 19309457.
103. Grefen C, Donald N, Hashimoto K, Kudla J, Schumacher K, Blatt MR. A ubiquitin-10 promoter-based vector set for fluorescent protein tagging facilitates temporal stability and native protein distribution in transient and stable expression studies. *The Plant journal: for cell and molecular biology*. 2010; 64(2):355–65. <https://doi.org/10.1111/j.1365-313X.2010.04322.x> PMID: 20735773.
104. Sparkes IA, Runions J, Kearns A, Hawes C. Rapid, transient expression of fluorescent fusion proteins in tobacco plants and generation of stably transformed plants. *Nat Protoc*. 2006; 1(4):2019–25. <https://doi.org/10.1038/nprot.2006.286> PMID: 17487191.
105. Peart JR, Lu R, Sadanandom A, Malcuit I, Moffett P, Brice DC, et al. Ubiquitin ligase-associated protein SGT1 is required for host and nonhost disease resistance in plants. *Proceedings of the National Academy of Sciences of the United States of America*. 2002; 99(16):10865–9. <https://doi.org/10.1073/pnas.152330599> PMID: 12119413; PubMed Central PMCID: PMC125064.
106. Izeddin I, Boulanger J, Racine V, Specht CG, Kechkar A, Nair D, et al. Wavelet analysis for single molecule localization microscopy. *Opt Express*. 2012; 20(3):2081–95. <https://doi.org/10.1364/OE.20.002081> PMID: 22330449.
107. Racine VH, A. Jouanneau, J. Salamero, J. Kervrann C., Sibarita., JP. MULTIPLE-TARGET TRACKING OF 3D FLUORESCENT OBJECTS BASED ON SIMULATED ANNEALING. *Conference Paper*. 2006. <https://doi.org/10.1109/ISBI.2006.1625094>
108. Claro E, Sarri E, Picatoste F. Measurement of phospholipase C activity in brain membranes. *Methods in molecular biology*. 1995; 41:177–88. <https://doi.org/10.1385/0-89603-298-1:177> PMID: 7655555.
109. Boudsocq M, Willmann MR, McCormack M, Lee H, Shan L, He P, et al. Differential innate immune signalling via Ca(2+) sensor protein kinases. *Nature*. 2010; 464(7287):418–22. <https://doi.org/10.1038/nature08794> PMID: 20164835; PubMed Central PMCID: PMC2841715.